

1 **A deeply conserved protease, acylamino acid-releasing enzyme (AARE), acts in ageing in**  
2 **Physcomitrella and Arabidopsis**

3 Sebastian N.W. Hoernstein<sup>1</sup>, Buğra Özdemir<sup>1,5</sup>, Nico van Gessel<sup>1</sup>, Alessandra A. Miniera<sup>1</sup>, Bruno  
4 Rogalla von Bieberstein<sup>1,6</sup>, Lars Nilges<sup>1</sup>, Joana Schweikert Farinha<sup>1,7</sup>, Ramona Komoll<sup>1,8</sup>, Stella  
5 Glauz<sup>1</sup>, Tim Weckerle<sup>1,9</sup>, Friedrich Scherzinger<sup>1,10</sup>, Marta Rodriguez-Franco<sup>2</sup>, Stefanie J. Müller-  
6 Schüssele<sup>3</sup>, Ralf Reski<sup>1,4,\*</sup>

7

8 <sup>1</sup> Plant Biotechnology, Faculty of Biology, University of Freiburg, Schaenzlestrasse 1, 79104  
9 Freiburg, Germany

10 <sup>2</sup> Cell Biology, Faculty of Biology, University of Freiburg, Schaenzlestrasse 1, 79104 Freiburg,  
11 Germany

12 <sup>3</sup> Molecular Botany, Department of Biology, Technical University of Kaiserslautern, Erwin-  
13 Schrödinger-Strasse 70, 67663 Kaiserslautern, Germany

14 <sup>4</sup> Signalling Research Centres BIOS and CIBSS, Schaenzlestrasse 18, 79104 Freiburg,  
15 Germany

16 <sup>5</sup> Euro-BioImaging Bio-Hub, EMBL Heidelberg, Meyerhofstraße 1, 69117 Heidelberg, Germany

17 <sup>6</sup> Department of Anesthesiology, University Hospital Würzburg, Oberduerrbacher Strasse 6,  
18 97072 Würzburg, Germany

19 <sup>7</sup> Institute for Molecular Biosciences, Goethe University Frankfurt, Max-von-Laue-Str. 9, 60438  
20 Frankfurt, Germany

21 <sup>8</sup> Heraeus Medical GmbH, Philipp-Reis-Straße 8-13. 61273 Wehrheim, Germany

22 <sup>9</sup> Eurofins GeneScan GmbH, Engesserstraße 4, 79108 Freiburg, Germany

23 <sup>10</sup> Centre for Integrative Biodiversity Research (iDiv) Halle-Jena-Leipzig, Puschstrasse 4, 04103  
24 Leipzig, Germany

25 \* Corresponding author: ralf.reski@biologie.uni-freiburg.de

26

27 **ORCID-IDs** S.N.W.H.: 0000-0002-2095-689X, B.Ö.: 0000-0001-9823-0581, N.v.G.: 0000-0002-  
28 0606-246X, A.A.M.: 0000-0003-1638-5438, B.R.v.B.: 0000-0002-9650-4064, L.N.: 0000-0003-

29 0716-7236, J.S.F.: 0000-0002-5602-3901, R.K.: 0000-0002-3142-0863, S.G.: 0000-0002-2305-  
30 4525, T.W.: 0000-0002-9584-5449, F.S.: 0000-0001-5825-6621, M.R.F.: 0000-0003-1183-2075,  
31 S.J.M.S.: 0000-0003-4061-1175, R.R.: 0000-0002-5496-6711

32 **Key words** aging, Physcomitrium, plant ageing, protein oxidation, ROS

33

34 **Abstract**

35 Reactive oxygen species (ROS) are constant by-products of aerobic life. In excess, ROS lead to  
36 cytotoxic protein aggregates, which are a hallmark of ageing in animals and linked to age-related  
37 pathologies in humans. Acylamino acid-releasing enzymes (AARE) are bifunctional serine  
38 proteases, acting on oxidized proteins. AARE are found in all domains of life, albeit under different  
39 names, such as acylpeptide hydrolase (APEH/ACPH), acylaminoacyl peptidase (AAP), or  
40 oxidized protein hydrolase (OPH). In humans, AARE malfunction is associated with age-related  
41 pathologies, while their function in plants is less clear. Here, we provide a detailed analysis of  
42 *AARE* genes in the plant lineage and an in-depth analysis of AARE localization and function in  
43 the moss *Physcomitrella* and the angiosperm *Arabidopsis*. *AARE* loss-of-function mutants have  
44 not been described for any organism so far. We generated and analysed such mutants and  
45 describe a connection between AARE function, aggregation of oxidized proteins and plant ageing,  
46 including accelerated developmental progression and reduced life span. Our findings complement  
47 similar findings in animals and humans, and suggest a unified concept of ageing may exist in  
48 different life forms.

49

## 50 Introduction

51 Reactive oxygen species (ROS) are by-products of O<sub>2</sub> metabolism and represent a challenge to  
52 all aerobic life. ROS play a dual role as potentially lethal oxidants and as signalling molecules<sup>1</sup>.  
53 Therefore, aerobic organisms possess sophisticated redox systems to scavenge and detoxify  
54 excess ROS. The major sources of ROS in plant cells are the electron transport chains in  
55 mitochondria and plastids, but also in peroxisomes and at the plasma membrane<sup>2</sup>. Environmental  
56 stresses such as heat, drought or intense light are factors for increasing ROS production to  
57 detrimental levels. Plants possess a repertoire of detoxifying enzymes such as catalases,  
58 superoxide dismutases, ascorbate peroxidases, glutathione peroxidase-like proteins and  
59 peroxiredoxins. Electrons for reduction are largely provided *via* non-enzymatic components such  
60 as ascorbic acid, glutathione and NADPH<sup>3,4,5,6,7</sup>. In addition, a range of heat-shock proteins assist  
61 in disaggregation or refolding of damaged proteins<sup>8,9,10</sup>.

62 Despite conversion into non-toxic derivatives, the continuous exposure to ROS results in oxidation  
63 of DNA, lipids, and proteins<sup>5</sup>. On the protein level, ROS lead to irreversible cysteine oxidation,  
64 advanced glycation end-products, adducts with ROS-generated reactive aldehydes, and  
65 carbonylation of amino-acid side-chains<sup>11,12</sup>. If not cleared *via* proteolysis, an excess of oxidized  
66 proteins accumulates to cytotoxic protein aggregates. Plant antioxidant systems and the role of  
67 ROS as signalling molecules in abiotic stress responses are well studied<sup>13</sup>. Yet, factors involved  
68 in a plant cell's last line of defence, such as the proteolytic systems for the clearance of irreversibly  
69 oxidized proteins, are still underexplored.

70 A class of serine proteases is evolutionary deeply conserved as their activity is found in bacteria,  
71 archaea, animals and plants, and can degrade irreversibly oxidized proteins<sup>14,15,16,17</sup>. These  
72 proteases have different names in different organisms, e.g. acylamino acid-releasing enzyme  
73 (AARE), acylpeptide hydrolase (APEH/ACPH), acylaminoacyl peptidase (AAP), or oxidized  
74 protein hydrolase (OPH)<sup>18</sup> but are collectively addressed as AARE here. AARE acts in multimeric  
75 complexes<sup>14,17</sup> as a bifunctional protease as it cleaves N<sup>α</sup>-acetylated amino acids from  
76 oligopeptides *via* an exopeptidase mode, but also cleaves oxidized proteins *via* an endopeptidase  
77 mode<sup>16,19,20,21,22</sup>. AARE isoforms from various organisms show different specificities towards N<sup>α</sup>-  
78 acetylated amino-acids, with bacterial and archaeal enzymes preferring AcLeu and AcPhe  
79 substrates<sup>15,23,24,25</sup> and plant and animal isoforms preferring AcAla, AcMet or AcGly  
80 substrates<sup>16,17,26,27</sup>. Besides substrate specificities, their subcellular localization appears to be  
81 conserved among eukaryotes, as human (HsACPH) and Arabidopsis (AtAARE) AAREs are  
82 reported as cytosolic enzymes<sup>20,21</sup>.

83 In humans, AARE malfunction is linked to different types of cancer<sup>26,28,29</sup> and sarcoma cell  
84 viability<sup>30</sup>. Moreover, AARE and proteasomal activity correlate and cooperatively prevent cytotoxic  
85 aggregate formation<sup>31,32,33</sup>. Several selective inhibitors have been identified<sup>34,35</sup> and blocking of  
86 AARE function is considered as anti-cancer treatment<sup>28</sup>. Despite an increasing number of studies  
87 on AARE functionality in humans, AAREs in plants are far less characterized.

88 AARE from *Arabidopsis thaliana* (AtAARE) and from cucumber have endo- and exopeptidase  
89 functions<sup>17</sup>, and silencing of *AtAARE* increased the levels of oxidized proteins<sup>21</sup>. AtAARE activity  
90 was also detected in plastid stroma fractions, although a fusion with a fluorescent reporter did not  
91 co-localize with chloroplasts<sup>21</sup>. Suppression of *AtAARE* via RNAi resulted in an enhanced  
92 accumulation of oxidized proteins in roots and enhanced electrolyte leakage in leaves, but a  
93 further impact on plant physiology was not described<sup>21</sup>.

94 Moreover, the complete loss of function of this protease has not yet been reported for any  
95 organism, neither bacterium, archaeon, animal, or plant. Thus, although the deep evolutionary  
96 conservation of AARE suggests its pivotal role in all major life forms, experimental evidence is far  
97 from optimal.

98 In a proteomics study on protein arginylation we identified an AARE homolog from the moss  
99 *Physcomitrella*<sup>36</sup>. Our further analysis revealed altogether three *Physcomitrella* AARE homologs  
100 (PpAARE1-3). Here, we analysed the subcellular localization of these PpAARE isoforms and of  
101 their homolog from the angiosperm *Arabidopsis* (AtAARE). We show that an alternative splicing  
102 event is targeting PpAARE1 to chloroplasts, mitochondria and the cytosol. We provide evidence  
103 that an alternative translation initiation is sufficient to localize AtAARE to the same three  
104 subcellular compartments. Bioinformatic analyses of several genomes suggest that the  
105 localization of AARE in chloroplasts and mitochondria is conserved across the plant lineage.  
106 Employing combinatorial gene knockouts and protein co-immunoprecipitation we found distinct  
107 interactions between these three isoforms and their concerted action on progressive ageing in  
108 *Physcomitrella*. Likewise, an *Arabidopsis* AARE loss-of-function mutant exhibits enhanced levels  
109 of oxidized proteins and accelerated bolting, as a hallmark of plant ageing.

110

## 111 Results

### 112 **AARE gene family expansion and splice variants**

113 Previously, PpAARE1 (Pp1s619\_3V6.1) was identified as the most prominent target for N-  
114 terminal arginylation in *Physcomitrella*<sup>36,37</sup>. N-terminal arginylation mediates poly-ubiquitination  
115 via the N-degron pathway, thus triggering subsequent proteasomal degradation<sup>38</sup>.  
116 Simultaneously, two homologs (PpAARE2: Pp1s108\_134V6.1 and PpAARE3: Pp1s97\_68V6.1)  
117 were identified, although those were not proven arginylation targets<sup>36</sup>. Meanwhile, a new  
118 *Physcomitrella* genome version with chromosome assembly and updated gene versions was  
119 released<sup>39</sup>. Consequently, the gene accessions used here are *PpAARE1* (Pp3c2\_30720V3.1),  
120 *PpAARE2* (Pp3c12\_21080V3.1), and *PpAARE3* (Pp3c7\_25140V3.1). According to  
121 *OrthoMCL*<sup>40,41</sup>, all three proteins are homologs of the *Arabidopsis thaliana* acylamino acid-  
122 releasing enzyme (AtAARE: AT4G14570). According to publicly available data  
123 (<https://peatmoss.online.uni-marburg.de>)<sup>42</sup> *PpAARE1-3* are expressed in all major *Physcomitrella*  
124 tissues and developmental stages, although at varying levels (Fig. S1a). Except for leaves  
125 (phylloids) and spores, *PpAARE1* is the most strongly expressed gene of this family (between 4  
126 and 20 times). In contrast, *PpAARE2* is expressed considerably stronger than *PpAARE1* and  
127 *PpAARE3* in spores (Fig. S1a). Likewise, *AtAARE* is expressed in all major *Arabidopsis* tissues  
128 (Fig. S1b, data utilized from Mergner et al. (2020)<sup>43</sup> and downloaded from  
129 <http://athena.proteomics.wzw.tum.de/>). These data indicate a strong, positive correlation between  
130 transcript level and protein abundance across all tissues (Fig. S1b). Stress conditions decrease  
131 *AARE* expression in *Arabidopsis* shoots and in *Physcomitrella protonemata* (Fig. S1c-e).

132 To investigate whether other plants also possess multiple AARE homologs and to infer their  
133 phylogenetic relation, we conducted *BLASTP*<sup>44</sup> searches against protein models from selected  
134 species using the protein sequence of *AtAARE* as a query. We selected the alga *Chlamydomonas*  
135 *reinhardtii*<sup>45</sup>, the liverwort *Marchantia polymorpha*<sup>46</sup>, the peat moss *Sphagnum fallax* (*Sphagnum*  
136 *fallax* v1.1, DOE-JGI, <http://phytozome.jgi.doe.gov/>), the lycophyte *Selaginella moellendorffii*<sup>47</sup>,  
137 the monocot *Oryza sativa*<sup>48</sup> and the dicot *Populus trichocarpa*<sup>49</sup>, all available at the Phytozome12  
138 database (<https://phytozome.jgi.doe.gov>). Additionally, we performed a NCBI *BLASTP* search  
139 against the charophyte *Klebsormidium nitens* proteome<sup>50</sup>, and identified a single homolog  
140 (GAQ80280.1) in this species. We also included proteins of *Funaria hygrometrica*<sup>51</sup>, a close  
141 relative to *Physcomitrella* from the Funariaceae family<sup>52</sup>, in our search. Finally, the *AtAARE*  
142 sequence was again searched against the *Physcomitrella*<sup>39</sup> and *Arabidopsis*<sup>53</sup> proteomes.

143 Homology of the resulting *BLAST* hits was confirmed if the reciprocal best *BLAST* hit against *A.*  
144 *thaliana* was again AtAARE.

145 In *P. trichocarpa*, we identified a single homolog for which three distinct splice variants are  
146 annotated (Potri.008G160400.1, Potri.008G160400.2, Potri.008G160400.3). These encode  
147 different protein isoforms, but two variants seem to encode non-catalytic proteins. AARE enzymes  
148 are prolyl-oligopeptidases with a conserved catalytic triad (Ser/Asp/His) in the C-terminal  
149 peptidase domain<sup>54,55</sup>. In splice variant 2 (Fig. S2, Potri.008G160400.2) alternative splicing results  
150 in the deletion of the catalytic Asp whereas the whole catalytic triad is lacking in splice variant 3  
151 (Potri.008G160400.3). Hence, we consider these splice variants as non-active and disregard  
152 them from further discussion.

153 In rice, we identified two homologs (LOC\_Os10g28020.3, LOC\_Os10g28030.1), with an  
154 additional splice variant (LOC\_Os10g28020.1) at one locus which encodes an N-terminal  
155 extension.

156 In *C. reinhardtii*, *M. polymorpha*, *S. fallax* and *S. moellendorffii*, we identified a single ortholog  
157 each. In *M. polymorpha*, three distinct splice variants are annotated (Mapoly0111s0036.1,  
158 Mapoly0111s0036.2, Mapoly0111s0036.3). The latter two are UTR (untranslated region) splice  
159 variants, thus resulting in the same protein sequence, whereas Mapoly0111s0036.1 encodes an  
160 N-terminal extension of 97 aa compared to the other two variants. In *F. hygrometrica* we identified  
161 three distinct isoforms.

162 Finally, our *BLASTP* searches using the latest Physcomitrella protein models<sup>39</sup> confirmed three  
163 homologs of AtAARE (Pp3c2\_30720V3.1, Pp3c12\_21080V3.1, Pp3c7\_25140V3.1). Additionally,  
164 this search revealed another hit, Pp3c1\_2590V3.1. This gene is composed of a single exon and  
165 encodes a 131 aa protein which harbours the AARE N-terminal domain (PF19283). However, it  
166 lacks a catalytic peptidase domain and is hardly expressed across different culture conditions and  
167 tissues<sup>56</sup>. We also did not find any proteomics evidence across several Physcomitrella  
168 analyses<sup>36,57,58,59</sup> for this protein. Therefore, we excluded this gene from further analysis.

169 We then used phylogenetic reconstruction to investigate the origin of gene duplications within the  
170 gene family. As an outgroup, we included the well-characterized rat<sup>16</sup> and human<sup>26</sup> AARE and  
171 two isoforms of the Antarctic icefish *Chionodraco hamatus*<sup>27</sup>. Physcomitrella and *F. hygrometrica*  
172 share three distinct pairs of orthologs hinting at an expansion in the common ancestor of the two  
173 species. Our phylogenetic analysis did not resolve AARE subfamilies across kingdoms (Fig. 1a)

174 and we conclude that the gene family expansions observed in rice and in the Funariaceae are  
175 lineage-specific events.

176 In addition, this analysis reveals a closer relationship between *PpAARE1* and *PpAARE3*, which  
177 presumably originate from a more recent gene duplication event, compared to *PpAARE2*. This is  
178 supported by the fact that the open reading frames (ORFs) of *PpAARE1* and *PpAARE3* are  
179 represented by a single exon whereas the ORF of *PpAARE2* is split across 17 exons, similar to  
180 *AtAARE* (Fig. 1b). This is in congruence with a more recent emergence of intron-poor genes in  
181 intron-rich families linked to stress response and developmental processes<sup>60</sup> and in line with  
182 intron-less orphan *Physcomitrella* genes as earliest responders to abiotic stress<sup>61</sup>.

183 For the three *PpAARE* genes, several splice variants are annotated, but only two splice variants  
184 of *PpAARE1* give rise to distinct protein isoforms (Fig. 1b; PpAARE1\_1, PpAARE1\_2). Both splice  
185 variants are present in *Physcomitrella* protonema (Fig. 1b, c), according to RT-PCR with splice  
186 variant-specific primers (Supplementary Table S1). Likewise, for *AtAARE* two different ORF  
187 definitions exist. With Araport11<sup>62</sup>, a new version of the gene model was introduced exhibiting a  
188 longer ORF at the 5' end (Fig. 1b). We detected the full-length transcript *via* reverse transcription  
189 polymerase chain reaction (RT-PCR, Fig. 1c).

190 For *PpAARE1*, alternative splicing in the 5' end results in an N-terminal truncated variant whereas  
191 the longer non-spliced variant encodes an N-terminal plastid transit peptide (cTP) according to  
192 *TargetP2.0*<sup>63</sup>. A cleavage of the transit peptide at the predicted cleavage site (Ala<sup>72</sup>-M<sup>73</sup>,  
193 Supplementary Table S2) of PpAARE1 would release exactly the protein encoded by the short  
194 splice variant. In contrast, PpAARE2 and PpAARE3 do not harbour any predicted N-terminal  
195 targeting signals. Moreover, PpAARE3 is also lacking the WD40 domain that is present in  
196 PpAARE1 and PpAARE2 (Fig. 1d).

197 The extension of the originally annotated ORF of *AtAARE* also encodes a plastid transit peptide  
198 (Fig. 1d). To our knowledge, the longer variant of *AtAARE* has not yet been investigated, whereas  
199 the short variant of *AtAARE* localizes to the nucleus and the cytosol<sup>21</sup>. In agreement with the latter  
200 findings, we could predict a nuclear localization sequence (NLS, KKKK) with *LOCALIZER*<sup>64</sup>. Thus,  
201 targeting of *AtAARE* to the cytosol and the nucleus, but also to plastids could be enabled by  
202 alternative translation initiation. Likewise, *PtAARE* harbours a plastid transit peptide and a  
203 potential alternative translation initiation site downstream of the predicted cTP cleavage site.

204 Accordingly, we checked for NLS in PpAARE isoforms and found one (KRRP, Supplementary  
205 Table S2) in PpAARE1 and PpAARE3, whereas PpAARE2 has none, further supporting our

206 hypothesis that PpAARE1 and PpAARE3 originate from a relatively recent gene duplication event.  
207 Accordingly, alternative splicing also generates two distinct transcripts for AARE1 in rice  
208 (OsAARE1, Supplementary Table S2), where one variant encodes a potential plastid transit  
209 peptide.

210 For all other plant species, no plastid targeting sequence was predicted, while the *C. reinhardtii*  
211 AARE harbours a mitochondrial targeting sequence (Supplementary Table S2).

## 212 **PpAARE1 and AtAARE in mitochondria, chloroplasts and cytoplasm**

213 Organellar targeting of AARE has not yet been reported, although AARE activity was observed in  
214 plastid-enriched fractions of cucumber<sup>17</sup>. However, chloroplasts, peroxisomes and mitochondria  
215 are major hubs of ROS generation<sup>65</sup>, and thus are likely organelles with elevated levels of oxidized  
216 proteins. Thus, we investigated whether PpAARE1 and AtAARE would localize to chloroplasts *in*  
217 *vivo*.

218 We generated fusion constructs of the PpAARE isoforms and of AtAARE with eGFP for transient  
219 expression in *Physcomitrella* protoplasts. Due to the presence of a predicted plastid targeting  
220 peptide for PpAARE1, eGFP was fused in frame to the 3' end of all coding sequences (CDS).  
221 Since also peroxisomes are ROS-producing organelles, we used *PlantPredPTS1*<sup>66,67</sup> to check for  
222 the presence of C-terminal positioned peroxisomal targeting signals. None of the selected AARE  
223 isoforms were predicted to localize to peroxisomes (Supplementary Table S2). Although AtAARE  
224 has a C-terminal CKL tripeptide, which is experimentally verified to mediate peroxisomal  
225 targeting<sup>66,68</sup>, the properties of its other C-terminal amino acids most likely prevent peroxisomal  
226 targeting. A more recent prediction approach for PTS1-mediated targeting for Arabidopsis  
227 proteins<sup>69</sup> further supports this conclusion. Peroxisomal targeting can also be mediated *via* N-  
228 terminal nona-peptides<sup>70,71</sup>, but these motifs are also not present within the first 100 aa in any of  
229 the selected AARE sequences. In agreement with these predictions eGFP was fused to the 3'  
230 end of the CDSs.

231 For PpAARE1 three different fusion constructs were assembled. Among these, a fusion of the  
232 CDS of the short splice variant (Pp3c2\_30720V3.1) and eGFP was cloned, as well as a fusion of  
233 the CDS of the longer splice variant (Pp3c2\_30720V3.2) and eGFP. Additionally, we cloned a  
234 fusion of eGFP and the sequence part in which both variants differ (M<sup>1</sup>-A<sup>72</sup>, Pp3c2\_30720V3.2).  
235 This part harbours the plastid transit peptide predicted by *TargetP2.0*. All fusion constructs were  
236 expressed under the control of the *Physcomitrella* Actin5 promoter<sup>57,72</sup> in a pMAV4 plasmid  
237 backbone<sup>73</sup>.



238 The PpAARE1 isoform derived from the short splicing variant (PpAARE1\_1, Fig. 1b) clearly  
239 localized to the cytoplasm (Fig. 2). The same localization was observed for PpAARE2 and  
240 PpAARE3 (Fig. 2). Despite a predicted NLS, we did not observe a nuclear localization, either for  
241 PpAARE1 or for PpAARE3.

242 The isoform encoded by the longer splice variant of *PpAARE1* (PpAARE1\_2, Fig. 1b) localized to  
243 chloroplasts and surprisingly also to mitochondria (Fig. 2). In contrast to the diffuse cytosolic  
244 distribution of PpAARE1, specific foci were observed in chloroplasts. To investigate whether the  
245 N-terminal sequence differing between the two PpAARE1 variants (M<sup>1</sup>-A<sup>72</sup>, Pp3c2\_30720V3.2) is  
246 sufficient to confer dual targeting, we fused this N-terminal sequence 5' to eGFP and observed  
247 again dual localization (Fig. 2, PpAARE1\_Nt). Full-length PpAARE1 was necessary to localize  
248 eGFP to foci within chloroplasts, as the PpAARE1\_Nt:eGFP fusion led to a uniform distribution.  
249 However, full-length PpAARE1 was also homogeneously distributed throughout the cytoplasm.  
250 This indicates the presence of interactors that recruit PpAARE1 to specific sites or complexes  
251 within the chloroplasts. Further, we conclude that the N-terminal extension of PpAARE1\_2  
252 encodes an ambiguous targeting signal for import into chloroplasts and mitochondria as it is  
253 capable of directing the fusion protein simultaneously to both organelles.

254 Simultaneous localization of proteins to chloroplasts and mitochondria can be mediated *via*  
255 ambiguous targeting signals which are recognized by both translocation machineries. We  
256 evaluated whether *ATP2*<sup>75</sup>, a tool for the prediction of ambiguous targeting, would recognize  
257 PpAARE1 but this was not predicted to be dually targeted. In contrast, AtAARE was predicted to  
258 be dually targeted *via* an ambiguous signal. Thus, we cloned the analogous three fusion  
259 constructs for AtAARE and investigated the subcellular localization of their encoded proteins  
260 accordingly.

261 The AtAARE isoform translated from the shorter ORF (AtAARE, Fig. 1b) localized to the  
262 cytoplasm (AtAARE\_SV, Fig. 2), as observed for PpAARE1\_1. This result is partially in agreement  
263 with Nakai et al. (2012)<sup>21</sup> since we could not observe nuclear localization. Using the fusion  
264 construct of the longer AtAARE variant, we observed clear dual targeting of the protein to  
265 chloroplasts and mitochondria (AtAARE\_LV, Fig. 2), as observed for PpAARE1\_2. Here, the  
266 eGFP signal was distributed homogeneously in the chloroplasts, in contrast to the foci of  
267 PpAARE1:eGFP.

268 Next, we cloned only the N-terminal sequence differing between both variants (M<sup>1</sup>-A<sup>55</sup>, longer  
269 ORF definition, Fig. 1b) and fused it to eGFP. In order to investigate whether the exact N-terminal

270 difference between the two AtAARE variants would be sufficient for targeting, the M<sup>56</sup> (same as  
271 M<sup>1</sup> in the shorter variant), which is the P1 aa at the predicted cleavage site, was deleted. Using  
272 this construct, the eGFP signal localized to chloroplasts and mitochondria (AtAARE\_Nt, Fig. 2).  
273 The signal within chloroplasts was homogeneously distributed, similar to the longer AtAARE  
274 variant. Thus, we conclude that the N-terminal extension of both long PpAARE and AtAARE  
275 variants is sufficient for dual targeting of proteins *in vivo*. Intriguingly, the longer variant of AtAARE  
276 localized exclusively to chloroplasts and mitochondria although alternative translation initiation  
277 should be possible. This is interesting as alternative translation initiation is also possible in the  
278 longer splice variant of *PpAARE1* (*PpAARE1\_2*). In the latter also, the fusion protein localizes  
279 exclusively to chloroplasts and mitochondria, which excludes the possibility of an alternative  
280 translation initiation, at least in protoplasts. There are numerous transcripts in mammals where  
281 translation of an upstream positioned ORF suppresses the translation of the downstream main  
282 ORF<sup>76</sup>. A similar scenario is conceivable in *Physcomitrella*. However, it remains unclear how and  
283 if translation from the internal start codons is controlled. It is also possible that factors controlling  
284 alternative translation initiation of AtAARE are absent in *Physcomitrella*, at least in a  
285 spatiotemporal manner, or they might only be triggered in specific physiological situations.  
286 According to our data, the translation of the two variants of *PpAARE1* is mainly controlled by  
287 alternative splicing and not by alternative translation initiation.

288 In summary, *PpAARE1* and *AtAARE* localize to three subcellular compartments *via* an ambiguous  
289 targeting signal. In contrast, *PpAARE2* and *PpAARE3* localize solely to the cytoplasm.

290

### 291 **Double knockout of *PpAARE1/2* reduces lifespan**

292 Null mutants of *AARE* have not been described in any organism, and the biological role of this  
293 protease apart from its catalytic function remained unclear. Hence, we created *AARE* knockouts  
294 in *Physcomitrella* by deleting the full CDS of each gene *via* gene targeting (Fig. 3a) according  
295 to<sup>77</sup>. To enable subsequent knockout (KO) of other *AARE* genes, different selection markers were  
296 used. Since three distinct *AARE* genes exist in *Physcomitrella* which result in cytosolic proteases,  
297 we generated all possible combinations of double KOs and triple KOs to avoid potential  
298 compensation of the loss of function.

299 Plants surviving the selection procedure were screened *via* PCR for the absence of the respective  
300 CDS and correct integration of the KO construct in the target locus (Fig. S4a). Additionally, the  
301 number of genomic integrations of the KO construct was measured *via* quantitative PCR (qPCR)

302 as described<sup>78</sup> (Fig. S4b). At least three independent lines were identified for all single, double  
303 and triple KOs (Fig. S4c-i) and a line with only a single integration in the genome was detected  
304 for each KO (j-p, line numbers with stars). Further, haploidy of all lines was confirmed *via* flow  
305 cytometry (Fig. S5a-c) as described<sup>79</sup>. These precautions were made as the transformation  
306 procedure may generate plants with multiple integrations<sup>80</sup>, possibly leading to off-target effects.  
307 Further, the transformation procedure may lead to diploid plants with altered gene expression<sup>81</sup>.  
308 We used haploid lines with a single integration of the KO construct (Fig. S4) for subsequent  
309 experiments.

310 Typically, AARE exopeptidase activity is assayed *via* N<sup>α</sup>-acetylated amino acids like AcAla or  
311 AcMet coupled to a reporter such as para-nitro-anilide (pNA) or 7-amido-4-methylcoumarin  
312 (AMC). From these, AcAla-pNA was tested for several eukaryotic AAREs<sup>22,26</sup>, including  
313 AtAARE<sup>17</sup>. Here, we analysed the impact of AARE loss of function on the activity towards AcAla-  
314 pNA and AcLeu-pNA. The latter is a substrate of bacterial and archaeal AARE isoforms but also  
315 eukaryotic isoforms exhibit cleavage activity on this substrate<sup>16,22,23,24,25</sup>. On the single KO level,  
316 the exopeptidase activity on both substrates was significantly reduced in the  $\Delta PpAARE1$  mutant  
317 whereas the single KO of the other isoforms did not affect the activity (Fig. 3b). This strong impact  
318 of PpAARE1 on the exopeptidase activity was consistent across all transgenic mutant lines (Fig.  
319 S6).

320 One important step in *Physcomitrella* development is the transition from protonema to  
321 gametophores, a developmental progression regulated among others by plant age and the  
322 nutrient status<sup>82</sup>. The single KOs were phenotypically inconspicuous on the gametophore level  
323 (Fig. 3c). In contrast, gametophores of  $\Delta PpAARE1/2$  and  $\Delta PpAARE1/3/2$  were severely stunted  
324 and colonies were denser compared to wild type (WT) or the other mutants (Fig. 3c). This growth  
325 effect is restricted to gametophores since protonema growth on solid medium did not differ  
326 between WT and the KOs (Fig. 3d, e). Intriguingly,  $\Delta PpAARE1/2$  and  $\Delta PpAARE1/3/2$  mutants  
327 showed accelerated developmental transition, as they developed gametophores from protonema  
328 earlier (Fig. 3d). Since other KO lines did not show this effect, we attributed this to the double KO  
329 of *PpAARE1/2* and performed a quantitative comparison with WT. Here, gametophores were  
330 already observed after 6 days in the double KO of *PpAARE1/2*, while in WT a similar number of  
331 gametophores per colony was observed only after 13 days (Fig. 3f). Consequently, the double  
332 KO of *PpAARE1/2* causes accelerated developmental progression but gametophores remained  
333 ultimately smaller than in WT (Fig. 3c). These effects are not linked to AARE exopeptidase activity

334 since the exopeptidase activity in gametophores was significantly reduced in all lines with a KO  
335 of PpAARE1 (Fig. 3g), which mimics the activity profile in protonema (Fig. S6).

336 To analyse AARE endopeptidase activity, we assessed the total levels of oxidized proteins in  
337 gametophores. In this assay, protein carbonyl groups derived from oxidation are derivatized with  
338 2,4-dinitrophenylhydrazine (DNPH) to 2,4-dinitrophenylhydrazone (DNP). This irreversible  
339 modification is then recognized on Western blots by a primary anti-DNP antibody. Since DNPH  
340 can also react with oxidation states of cysteine side chains<sup>83</sup>, this assay detects not only protein  
341 carbonylation but general protein oxidation.

342 With this assay we found that PpAARE2 had the strongest impact on the level of oxidized proteins  
343 in gametophores (Fig. 3h) and thus is not linked to exopeptidase activity. This was consistently  
344 observed in three independent analyses (Fig. 3h, Fig. S7). Apparently, PpAARE3 does not have  
345 any impact on exopeptidase and endopeptidase activity in gametophores under standard  
346 conditions (Fig. 3g, h).

347 Taken together, PpAARE1 predominantly acts as exopeptidase, while PpAARE2 predominantly  
348 acts as endopeptidase, and only the simultaneous loss of both activities in the double knockout  
349 mutants has the severest phenotypical consequences.

350 We found another remarkable difference between WT and mutants with a double KO of  
351 *PpAARE1/2* in older plants. After 5 months of cultivation,  $\Delta PpAARE1/2$  and  $\Delta PpAARE1/3/2$  were  
352 only viable at the tip of the gametophores (Fig. 4a), whilst most of the colony was already dead.  
353 In contrast, gametophores of WT and the other KOs were fully viable. After 8 months,  
354  $\Delta PpAARE1/2$  and  $\Delta PpAARE1/3/2$  were already dead, in contrast to WT and the respective  
355 parental lines, which only showed some dead gametophores (Fig. 4b, c).

356 In summary, mutants with a double KO of *PpAARE1/2* exhibit accelerated developmental  
357 transition from protonema to gametophore (Fig. 3f), while size and life span of gametophores is  
358 strikingly reduced (Fig. 3c, Fig. 4a-c). In contrast, these effects are not visible in  $\Delta PpAARE1/3$ .  
359 Therefore, these ageing phenotypes are linked to the concurrent loss of major AARE  
360 endopeptidase and exopeptidase activity.

### 361 **Distinct *in vivo* interactions of PpAARE isoforms**

362 In different organisms, AARE forms different homomeric complexes such as dimers<sup>14</sup>,  
363 tetramers<sup>17</sup>, or hexamers<sup>24</sup>. Thus, we analysed whether the PpAARE isoforms can interact with  
364 each other. Previously, all three isoforms were identified, although the protein modification used

365 for pulldown (N-terminal arginylation) was only identified on PpAARE1<sup>36</sup>. This gave rise to two  
366 hypotheses: First, PpAARE2 and PpAARE3 are also targets for N-terminal arginylation, but  
367 modified peptides were not identified for these isoforms. Second, the isoforms interact in  
368 complexes which were pulled down due to the N-terminal arginylation of PpAARE1. We generated  
369 Citrine fusion lines for each isoform *via* in-frame tagging at the native locus (knock-in, Fig. 5a).  
370 The original stop codons of the respective PpAARE CDS were deleted. The Citrine-tag was  
371 intended for two different analyses: First, it should enable *in vivo* monitoring of PpAARE isoforms  
372 expressed from the native promoter, and second, it is a valid tag for co-immunoprecipitation (Co-  
373 IP) *via* commercially available trap-beads.

374 In plants with a detectable fusion transcript (Fig. S8a-c) the presence of the target protein was  
375 checked *via* IP and subsequent MS analysis. For *PpAARE3:Citrine* lines, we detected transcripts  
376 in one line and obtained only insufficient coverage and intensity at the MS across several Co-IPs.  
377 Thus, these *Physcomitrella* lines were excluded from further analysis. The co-precipitation of  
378 other PpAARE isoforms with the respective bait isoforms was observed in test IPs (Fig. S8d-e)  
379 confirming previous MS-Data<sup>36</sup>. All plants harbouring the Citrine fusion were phenotypically  
380 inconspicuous (Fig. S8f) and haploid (Fig. S8g). Although the fusion proteins were detected in  
381 two independent lines for each of the two isoforms (PpAARE1, PpAARE2), we could not observe  
382 any Citrine signal within *Physcomitrella* protonemata or gametophores, probably due to the low  
383 abundance of the PpAARE isoforms. Nevertheless, MS intensities and sequence coverage  
384 enabled quantitative Co-IPs. The MS data have been deposited in PRIDE with the accession  
385 codes PXD033854 and PXD038742<sup>84,85</sup>.

386 When targeting PpAARE1:Citrine, both other isoforms appeared as significant interacting  
387 partners (Fig. 5b,  $p < 0.01$ , FDR = 0.01). In a reciprocal Co-IP targeting PpAARE2:Citrine only,  
388 PpAARE1 appeared as significant interacting partner. PpAARE3 was not detected in this  
389 pulldown. Although lacking a reciprocal IP targeting PpAARE3:Citrine, the data show that  
390 PpAARE1 interacts with PpAARE2 and PpAARE3, whereas PpAARE2 only interacts with  
391 PpAARE1. Consequently, there are distinct interactions of PpAARE1 with PpAARE2 and  
392 PpAARE3 *in vivo*, possibly resulting in cytosolic heteromeric AARE complexes in *Physcomitrella*.

### 393 **AARE affects bolting time in Arabidopsis**

394 In *Physcomitrella* three AARE genes exist, and the concerted action and interaction of the  
395 enzymes affect plant ageing. To evaluate if this is an evolutionary conserved function, we  
396 analysed the situation in Arabidopsis. Here, it was known that silencing of the single AARE gene

397 leads to an accumulation of oxidized proteins, whereas overexpression did not affect their levels<sup>21</sup>.  
398 To gain deeper insights, we screened for available Arabidopsis T-DNA mutants.

399 We identified two T-DNA insertion lines (SALK\_071125 and GK-456A10) in the T-DNA Express  
400 database at the SIGnAL website (<http://signal.salk.edu>). SALK\_071125 (s68) has a T-DNA  
401 insertion in an intron at the 5'UTR, whereas the T-DNA insertion in GK-456A10 (GK) maps to an  
402 intron in the region encoding the catalytic domain (Fig. 6a). We obtained these mutants, identified  
403 homozygous populations of GK-456A10 containing the T-DNA insertion by their resistance to  
404 sulfadiazine, and confirmed their genotype by PCR. In the case of the Salk line (s68), homozygous  
405 plants had lost their resistance to kanamycin, but we confirmed their genotype by PCR.

406 Homozygous plants of both genotypes were back-crossed with WT Col-0, and brought to  
407 homozygosity for subsequent experiments. Primers for screening and validation of both T-DNA  
408 lines are listed in Supplementary Table S3. Additionally, we analysed *AARE* gene expression *via*  
409 RT-PCR. The transcript was still detectable in both lines (Fig. 6a), although very reduced in s68,  
410 while the protein was not detectable *via* Western blot (Fig. 6b). Surprisingly, in WT *AARE* was  
411 detected at around 100 kDa, although the estimated molecular weight is approximately 84 kDa  
412 (90 kDa for the longer ORF variant without cleavage of the plastid targeting peptide) which  
413 indicates the presence of posttranslational modifications. Phenotypically, neither seedlings nor  
414 adult mutant plants showed obvious deviations from WT (Col, Fig. S9)

415 Next, we assayed *AARE* exopeptidase function in Arabidopsis WT and the two mutants. The  
416 exopeptidase activity on AcAla-pNA was significantly reduced in both T-DNA mutants. In contrast,  
417 the activity on AcLeu-pNA did not change significantly, although a slight reduction was observed  
418 in the GK line (Fig. 6c). Thus, in agreement with Western blot and activity data, the remaining  
419 transcripts detected *via* RT-PCR (Fig. 6a) are not translated to functional enzymes, suggesting  
420 complete loss of *AARE* function in the mutants. Based on this characterization, we concentrated  
421 on T-DNA mutant s68.

422 Subsequently, we assayed the *AARE* endopeptidase activity in Arabidopsis. The most striking  
423 feature reported were increased levels of oxidized proteins in *AARE*-silenced Arabidopsis plants<sup>21</sup>  
424 which is in line with our findings in *Physcomitrella* *AARE* mutants. To corroborate this, we  
425 investigated levels of oxidized proteins in the Arabidopsis T-DNA mutant (s68) in comparison to  
426 WT (Col) cultivated under short day conditions. In both genotypes, the distribution of oxidized  
427 proteins was different to *Physcomitrella* gametophores (Fig. 6d). Using the same extraction  
428 protocol, oxidized proteins in Arabidopsis were mainly of lower molecular weight, whereas in

429 Physcomitrella they were mainly at higher molecular weight (Fig. 3h). Despite these size  
430 differences, the level of oxidized proteins was higher in the Arabidopsis mutant than in WT (Fig.  
431 6d), mimicking the situation in Physcomitrella. Together, we found AtAARE exopeptidase and  
432 endopeptidase activity to be reduced in our experiments.

433 Oxidized proteins accumulate during vegetative growth of Arabidopsis and are depleted at the  
434 transition to bolting<sup>86</sup>. It was not clear from this study whether the level of oxidized proteins is a  
435 signal for bolting, or if the reset of protein oxidation at the bolting transition is a side-effect of  
436 enhanced protein turnover during this process. To address this, we assessed the bolting  
437 behaviour of Arabidopsis WT and mutant plants and found that bolting in mutant plants differed  
438 significantly from WT. In WT, bolting started at 24±1 rosette leaves whereas it started at 21±2  
439 rosette leaves in the mutants (Fig. 6e). Consequently, this accelerated developmental transition  
440 in the mutants correlates with enhanced levels of oxidized proteins.

441

## 442 **Discussion**

443 A universal definition of ageing is difficult due to strongly differing characteristics between and  
444 within the domains of life. In humans, the term ageing is inherently linked to degenerative diseases  
445 whereas plant ageing is considered as the progression of developmental transitions from seeds  
446 to senescence. Nevertheless, a common feature of ageing is the execution of a genetic program  
447 that controls growth, development and maturation. In turn, the progression of this genetic program  
448 depends on the metabolic state and environmental factors. Among the molecules responsible for  
449 ageing are ROS. Their involvement in ageing and diseases was first postulated by Harman<sup>87</sup> and  
450 was extended by considering mitochondria as central sources<sup>88</sup>. In humans, mitochondrial  
451 malfunction in line with increased ROS levels is a central determinant of ageing and associated  
452 pathologies<sup>89</sup>. In plants, mitochondrial ROS increase during ageing of seeds<sup>90</sup> and are major  
453 determinants of germination capacity<sup>91</sup>. In photosynthetic tissues chloroplasts are the major  
454 source of ROS and their levels increase during ageing<sup>92,93,94</sup>. Plants cannot escape from stress  
455 situations that increase ROS production to detrimental levels, and despite several layers of ROS  
456 defence, oxidized proteins constitute the major share of modified molecules under stress.  
457 Consequently, protein oxidation and subsequent aggregate deposition are hallmarks of  
458 ageing<sup>95,96</sup>. The degradation of artificially oxidized proteins by AARE has been demonstrated  
459 repeatedly, and silencing of *AtAARE* in turn increased the levels of oxidized proteins<sup>19,20,21,22</sup>.

460 However, the contribution of AARE to the progress of ageing remained elusive, although several  
461 studies associate AARE-function to age-related diseases<sup>97,98,99</sup>. Here, we identified three *AARE*  
462 genes in *Physcomitrella*. This gene family expansion is an outstanding feature of the moss family  
463 Funariaceae, as most organisms we analysed contain only a single *AARE* gene, and only a few  
464 have two. We analysed these three isoforms in *Physcomitrella* and compared selected features  
465 to the single isoform in *Arabidopsis*. Our data reveal specific functions in age-related  
466 developmental transitions and life span determination.

467 Surprisingly, we found triple localization of AtAARE and PpAARE1 to chloroplasts, mitochondria  
468 and the cytosol *in vivo*, suggesting a functional role for AARE in these cellular compartments. In  
469 *Physcomitrella*, the triple localization is mediated *via* alternative splice variants and in *Arabidopsis*  
470 likely *via* alternative translation initiation. Although there have been indications of AtAARE being  
471 associated to chloroplasts<sup>17,21</sup>, there was no clear evidence for organellar targeting of this  
472 protease until now. It is remarkable that the triple localization of AARE is evolutionary conserved  
473 between *Arabidopsis* and *Physcomitrella*, although likely executed *via* different molecular  
474 mechanisms. This suggests an essential and evolutionary conserved function of AARE activity in  
475 the cytoplasm, chloroplasts and mitochondria. As mosses and seed plants diverged more than  
476 500 million years ago<sup>100</sup>, this is a deep evolutionary conservation.

477 Previously, AARE exopeptidase activity was observed in cucumber chloroplasts<sup>17</sup>, and AARE  
478 peptides were found in proteomes of *Arabidopsis* chloroplasts<sup>101</sup> and mitochondria<sup>102</sup>. In contrast,  
479 AARE was not identified in plastid or mitochondrial proteomes of *Physcomitrella*<sup>57,59</sup>. We found  
480 AARE exopeptidase activity in chloroplasts and mitochondria of *Physcomitrella*. Chloroplasts are  
481 a major source of ROS in photosynthetic tissues exposed to light, whereas mitochondria are the  
482 major source of ROS in non-photosynthetic tissues or in the dark<sup>93,94,103,104</sup>. Until now, it remained  
483 unresolved how plants deplete oxidized proteins from these organelles.

484 In yeast and mammals, the ATP-dependent LON and AAA proteases are involved in clearance  
485 of misfolded and oxidized mitochondrial proteins. Intriguingly, mutants of plant homologs of LON  
486 proteases did not show clear effects on the levels of oxidized proteins, but AAA-type FTSH  
487 proteases may play a role<sup>105</sup>. Nevertheless, stressors such as heat, drought or intense light  
488 compromise photosynthesis<sup>106,107</sup> and mitochondrial respiration<sup>108</sup>, leading to a depletion of ATP  
489 and to mitochondrial dysfunction<sup>109</sup>. In turn, energy supply for ATP-dependent defence systems  
490 such as heat-shock proteins and AAA-type proteases is severely compromised, leaving the  
491 question unanswered how oxidized proteins in chloroplasts and mitochondria can be cleared.  
492 Because AARE is an ATP-independent protease, our data suggest that organellar-targeted AARE



493 may act as an ATP-independent defence to prevent or attenuate protein aggregation in the major  
494 ROS-producing organelles.

495 Based on localization prediction, 70% of our selected plant species possess one AARE isoform  
496 that localizes to either plastids or to mitochondria. Whether dual targeting *via* ambiguous targeting  
497 also occurs in these species remains to be experimentally validated. Further, we do not exclude  
498 that the remaining species also have organellar AARE isoforms, because our predictions may be  
499 compromised by incomplete gene models. Such incomplete AARE gene models without a transit  
500 peptide were present in earlier genome annotations of Arabidopsis and Physcomitrella<sup>41,53</sup>, whilst  
501 complete gene models with transit peptides were only introduced with later versions<sup>39,62</sup>.

502 It is not yet clear how translation of both variants in Arabidopsis is regulated, but a recent study  
503 highlights the importance of alternative translation initiation in shaping different subcellular  
504 localizations or functions of proteoforms<sup>110</sup>. This mechanism is also present in Physcomitrella,  
505 where dual targeting of FtsZ isoforms to the cytoplasm and chloroplasts is enabled *via* alternative  
506 translation initiation<sup>111</sup>. Thus, localization of PpAARE1 to the cytoplasm is also possible from the  
507 longer splice variant. Alternative translation initiation of *AtAARE* is further evidenced by  
508 proteomics data ([www.peptideatlas.org/builds/arabidopsis/](http://www.peptideatlas.org/builds/arabidopsis/))<sup>112</sup>. Here, we found evidence for N-  
509 terminal acetylation of M<sup>56</sup> which is the initiator methionine of the short variant (PXD012708<sup>113</sup>).

510 A reporter fusion of the shorter *AtAARE* ORF was observed in the cytoplasm and in the nucleus<sup>21</sup>.  
511 We did not detect a nuclear localization of any AARE isoform. Using *LOCALIZER*<sup>64</sup> we identified  
512 an NLS in *AtAARE*, in PpAARE1 and PpAARE3, but not in PpAARE2. In contrast, the human  
513 AARE homolog HsACPH does not have a predictable NLS, but nuclear import is mediated *via*  
514 interaction with XRCC1 under stress, where it acts in DNA-damage repair<sup>114</sup>. Similarly, a nuclear  
515 localization of AARE might also occur under stress *in planta*.

516 In Physcomitrella, AARE1 is the dominant exopeptidase, whereas AARE2 acts predominantly as  
517 endopeptidase, and the operation mode of AARE3 remains unresolved. Crystal structures from  
518 bacterial and archaeal AAREs revealed two possible entrances for substrates to the catalytic  
519 centres<sup>14,115</sup> but the mode of substrate entry is not fully understood. Although the quaternary  
520 arrangements of subunits differ between species<sup>115,116</sup>, the secondary structure arrangement is  
521 conserved across kingdoms and specific subunit interactions (multimerization) are likely a  
522 mechanism to mediate substrate specificity and modulate activity. This could be further used as  
523 a switch between endopeptidase and exopeptidase activity and additionally enable access of the

524 catalytic centre *via* structural re-arrangements. Accordingly, the interaction between the distinct  
525 PpAARE isoforms may modify substrate specificity and activity.

526 Our data indicate a partial compensation between PpAARE1 and PpAARE2. Both single KO  
527 mutants are phenotypically inconspicuous under normal conditions, although a significant  
528 reduction in exopeptidase activity was observed in  $\Delta PpAARE1$ . PpAARE2 had the strongest  
529 effect on the accumulation of oxidized proteins in gametophores on the single isoform KO level,  
530 whereas the double KO of *PpAARE1* and *PpAARE2* showed the most striking effect in all lines  
531 as accelerated transition from protonema to gametophores. This phenotype is similar to mutants  
532 with disturbed auxin transport<sup>117</sup>. However, colony growth in these mutants was reduced which is  
533 different from our double KO mutant (*PpAARE1/2*). Intriguingly, this double KO results in stunted  
534 gametophores and a reduced life span. This phenotype partially resembles a loss-of-function  
535 mutant of a central component of autophagy (PpATG3) in *Physcomitrella*<sup>118</sup>. In  $\Delta PpATG3$ ,  
536 gametophores exhibit a reduced life span and colonies are smaller than in WT. In contrast,  
537 gametophore size was not affected. Further, photosynthetic capacity in  $\Delta PpATG3$  was also  
538 reduced, an effect which is apparently not caused by AARE depletion<sup>21</sup> and *PpAARE* genes were  
539 not differentially expressed in  $\Delta PpATG3$ <sup>118</sup>. We conclude that the reduced life span observed in  
540  $\Delta PpAARE1/2$  and  $\Delta PpAARE1/3/2$  is not due to an impaired autophagy system causing nitrogen  
541 starvation. This is in line with data which opposes autophagy at the onset of senescence in  
542 *Arabidopsis*<sup>119</sup>.

543 In mammals, elevated levels of oxidized proteins are associated with age-related pathologies,  
544 such as Alzheimer's disease, diabetes and different types of carcinomas<sup>120</sup>. If proteolytic  
545 clearance fails, further accumulation of oxidized proteins causes protein aggregation, which is a  
546 hallmark of ageing in animals<sup>96,121,122</sup>. A connection between protein oxidation and ageing was  
547 less well studied in plants. Plastid ROS levels increase during ageing<sup>92</sup>, which is in line with strong  
548 oxidation of plastid proteins in ageing leaves<sup>86</sup>. Likewise, protein oxidation marks the  
549 developmental transition between vegetative growth and flowering in *Arabidopsis*<sup>86</sup>.  
550 *Physcomitrella* mutants  $\Delta PpAARE1/2$  and  $\Delta PpAARE1/3/2$  showed accelerated developmental  
551 transition from protonema to gametophores, reduced life span and increased levels of oxidized  
552 proteins as signs of accelerated ageing. This is supported by the fact that gametophore tips, which  
553 is younger tissue, are viable longer than the older stems in both mutants. In the *Arabidopsis* *AARE*  
554 T-DNA mutants we found increased levels of oxidized proteins under normal cultivation conditions  
555 and an accelerated developmental transition, in this case premature bolting. These findings  
556 suggest an evolutionary conserved connection between protein oxidation and ageing.

557 We provide here a detailed analysis of *AARE* genes in the plant lineage and an in-depth analysis  
558 of AARE localization and function in the moss *Physcomitrella* and the annual angiosperm  
559 *Arabidopsis*. *AARE* loss-of-function mutants have not been described for any organism so far.  
560 We generated and analysed such mutants and describe a connection between AARE function,  
561 aggregation of oxidized proteins and plant ageing, including accelerated developmental  
562 progression and reduced life span. Our findings complement similar findings in humans and  
563 animals where AARE malfunction is associated with protein aggregation and age-related  
564 pathologies.

565 To solidify the role of AARE in ageing in different life forms, particularly in plants with contrasting  
566 maximum life spans and in animals of different complexity, loss-of-function mutants should be  
567 established and analysed in selected model species. Likewise, a deeper understanding of AARE-  
568 function in human diseases is desirable. Together, such analyses may contribute to a unified  
569 concept of ageing in different life forms.

570

## 571 **Methods**

### 572 Cultivation of *Physcomitrella*

573 *Physcomitrella* WT (new species name: *Physcomitrium patens* (Hedw.) Mitt.<sup>123</sup>); ecotype  
574 “Gransden 2004” and AARE KO lines were cultivated in Knop medium<sup>124</sup> supplemented with  
575 microelements. Knop medium (pH 5.8) containing 250 mg/L KH<sub>2</sub>PO<sub>4</sub>, 250 mg/L KCl, 250 mg/L  
576 MgSO<sub>4</sub> x 7 H<sub>2</sub>O, 1,000 mg/L Ca(NO<sub>3</sub>)<sub>2</sub> x 4 H<sub>2</sub>O and 12.5 mg/L FeSO<sub>4</sub> x 7 H<sub>2</sub>O supplemented with  
577 10 mL per litre of a microelement (ME) stock solution<sup>125,126</sup> (309 mg/L H<sub>3</sub>BO<sub>3</sub>, 845 mg/L  
578 MnSO<sub>4</sub> x 1 H<sub>2</sub>O, 431 mg/L ZnSO<sub>4</sub> x 7 H<sub>2</sub>O, 41.5 mg/L KI, 12.1 mg/L Na<sub>2</sub>MoO<sub>4</sub> x 2 H<sub>2</sub>O, 1.25 mg/L  
579 CoSO<sub>4</sub> x 5 H<sub>2</sub>O, 1.46 mg/L Co(NO<sub>3</sub>)<sub>2</sub> x 6 H<sub>2</sub>O). For cultivation on solid medium, 12 g/L Agar was  
580 added to the KnopME medium. Moss suspension cultures were disrupted weekly with an ULTRA-  
581 TURRAX (IKA) at 18,000 rpm for 90 s. If not indicated otherwise, moss was grown under standard  
582 light conditions (55 μmol photons/m<sup>2</sup>s) at 22°C in a 16h/8h light/dark cycle.

583 Hydroponic *Physcomitrella* gametophore cultures were assembled as described<sup>36,127</sup>. Here, a thin  
584 layer of protonema from suspension was distributed on gauze mesh (PP, 250 m mesh, 215 m  
585 thread, Zitt Thoma GmbH, Freiburg, Germany) capped on a glass ring. The glass rings with  
586 protonema-covered mesh gauze were placed in Magenta<sup>®</sup>Vessels (Sigma-Aldrich, St. Louis,  
587 USA) and KnopME medium was added until the protonema-covered gauze mesh was moist. The  
588 medium was exchanged every 4 weeks. Gametophores were harvested after 12 weeks.

589 Gametophore colonies on Agar plates (KnopME) were generated by transplanting single  
590 gametophores to new plates. Plates were sealed with Parafilm<sup>®</sup>.

### 591 Generation of AARE knockout lines

592 Knockout constructs for each *PpAARE* gene were generated by amplifying genomic regions as  
593 homologous flanks. The PCR products were fused to a neomycin (*PpAARE1*), hygromycin  
594 (*PpAARE2*) and zeocin (*PpAARE3*) resistance cassettes, respectively, employing triple template  
595 PCR as described<sup>128</sup> with primer sequences listed in Supplementary Table S1 using the Q5  
596 polymerase (New England Biolabs, Ipswich, USA). The knockout constructs were released from  
597 their vector backbones with XhoI (*PpAARE1*), BglII (*PpAARE2*) and DraI (*PpAARE3*),  
598 respectively. Enzymes were purchased from Thermo Fisher Scientific. Digested plasmids were  
599 precipitated and sterilized prior to transfection using standard ethanol precipitation method<sup>129</sup>.  
600 Transfection of *Physcomitrella* WT or KO (for consecutive knockouts) protoplasts was conducted  
601 via PEG-mediated procedure<sup>77,130</sup>. The WT strain as well as the identified *PpAARE* KO lines are

602 accessible via the International Moss Stock Center (IMSC, [www.moss-stock-center.org](http://www.moss-stock-center.org)). IMSC  
603 accession numbers for the mutant and WT are available in Supplementary Table S4.

604 Screening of plants surviving antibiotics selection was done by PCR. KO mutant plants surviving  
605 the antibiotics selection were checked for the presence of a genomic region which should be  
606 removed upon homologous recombination-based integration of the knockout construct (Fig. S4a).  
607 In case of the absence of this WT signal, plants were further checked for correct 5' and 3'  
608 integration of the respective knockout construct using primers listed in Supplementary Table S1.

#### 609 Protonema growth and gametophore induction

610 Suspension cultures were started at the same day and disrupted weekly as described. Dry weight  
611 was measured in triplicates and suspension density was adjusted to 440 dry weight (DW) per litre  
612 (mg DW/L) as described<sup>131</sup>. Droplets of 15  $\mu$ L were distributed on solid medium (Knop ME, 0.02%  
613 glucose). Sealed plates were cultivated as described above. Three droplets each per line were  
614 distributed on one plate and all lines were grown on the same plate. 3 plates (12 colonies) were  
615 used per assay. Colony areas were measured with *ImageJ*. White pixels counted from binarized  
616 colony images were used as quantitative values. Gametophores were counted upon visibility of  
617 the first leafy structure on buds.

#### 618 Generation of PpAARE-Citrine knock-in lines

619 Knock-in constructs to fuse the coding sequence of Citrine to the C-terminus of PpAARE isoforms  
620 via an 18 bp linker<sup>128</sup> at the endogenous genomic locus were cloned via Gibson assembly<sup>132</sup>. All  
621 necessary parts were amplified using primers listed in Supplementary Table S1. Additionally, XhoI  
622 (*PpAARE1*), Sall (*PpAARE2*) and BamHI (*PpAARE3*) restriction sites were added to the 5' and 3'  
623 ends of the respective knock-in construct. All parts were assembled into pJet1.2 vector backbone  
624 (Thermo Scientific) using the Gibson Assembly@Cloning Kit from New England Biolabs (Ipswich,  
625 Massachusetts, USA). Transfection of *Physcomitrella* WT protoplasts were conducted as  
626 described<sup>77,130</sup> by co-transfecting a plasmid containing a neomycin phosphotransferase  
627 resistance (nptII) cassette as transient selection marker (pBSNNNEV, Mueller et al., 2014)<sup>57</sup>. The  
628 linearized plasmid and the co-transfection vector were purified and sterilized *via* ethanol  
629 precipitation<sup>129</sup> prior to transfection.

630 The presence of Citrine was checked with primers listed in Supplementary Table S1 and resulting  
631 positive lines were further checked for correct 5' and 3' integration by PCR using the Plant Phire  
632 Kit with primers listed in Supplementary Table S1. All identified fusion lines are available *via* the

633 International Moss Stock Center (IMSC, [www.moss-stock-center.org](http://www.moss-stock-center.org)). IMSC accessions are  
634 listed in Supplementary Table S4.

#### 635 qPCR analysis

636 The copy number of the integrated KO constructs was determined using a qPCR-based method<sup>78</sup>.  
637 Genomic DNA was extracted from 100 mg frozen protonema using the GeneJET Plant Genomic  
638 DNA Purification Kit (Thermo Scientific, Waltham, USA). DNA concentrations were adjusted to 3  
639 ng/μl for each sample and qPCR was performed with primers for the 5' and 3' flanks as well as  
640 with primers for the corresponding selection cassette. Additionally, primers for the single copy  
641 gene *CLF* (Pp3c22\_2940V3) were used as internal control. Reference lines were WT as well as  
642 in-house lines with known single integrations of the used selection cassettes. Primers are listed  
643 in Supplementary Table S5. PCR reactions were done using 2x SensiFAST Mix (Bioline, London,  
644 UK) and analysed in a Lightcycler 480 II (Roche, Basel, Schweiz).

#### 645 cDNA preparation

646 RNA was extracted using the innuPREP Plant RNA Kit (Analytik Jena, Jena, Germany). The  
647 extracted RNA was treated with DNase I (Thermo Scientific) and subsequently reverse  
648 transcribed into cDNA using Superscript III Reverse Transcriptase (Life Technologies, Carlsbad,  
649 USA).

#### 650 Fusion constructs for subcellular localization

651 All constructs were generated using Gibson assembly<sup>132</sup> and integrated into a  
652 PpAct5:Linker:eGFP-MAV4 vector backbone<sup>73</sup>. Integration of the different coding sequences was  
653 done in frame in front of the Linker:eGFP. All parts for the Gibson assembly (inserts and  
654 corresponding vector backbones) were amplified either with Phusion<sup>TM</sup> polymerase (Thermo  
655 Fisher Scientific) or with HiFi polymerase (PCR Biosystems Ltd) according to the manufacturer's  
656 instructions. The primers were designed to have a 25 bp overlap to the corresponding fragment  
657 to be fused with. All primers and combinations are listed in Supplementary Table S6. In the case  
658 of the N-terminal difference of AtAARE (M1-A<sup>55</sup> of AT4G14570.1, gene model provided by TAIR  
659 (<https://www.arabidopsis.org/>)) the Actin5 promoter was replaced by the CaMV35S promoter<sup>133</sup>  
660 previously validated in *Physcomitrella*<sup>134</sup>.

661 Cloned plasmids were purified using the PureYield<sup>TM</sup> Plasmid Midiprep kit (Promega, Wisconsin,  
662 USA) according to the manufacturer's instructions. The plasmids were purified and sterilized *via*  
663 ethanol precipitation<sup>129</sup>.

## 664 Confocal microscopy

665 Confocal imaging was performed on transiently transfected live protoplasts using Leica TCS SP8  
666 (Leica Microsystems, Wetzlar, Germany). Immediately before microscopy, MitoTracker™ Orange  
667 CMTMRos (ThermoFisher Scientific) was added to protoplast suspensions to a final concentration  
668 of 100 nM. For all imaging experiments, an HC PL APO CS2 63x/1.40 OIL objective was used  
669 with a zoom factor of 4. The pinhole was set to 35.4 µm. For excitation, a WLL laser (70%) was  
670 used. In a sequential acquisition setup, eGFP and chlorophyll were excited with the same laser  
671 beam (488 nm, 2%) and their signals were detected simultaneously, whereas MitoTracker™ was  
672 excited with a different laser beam (550 nm, 2%) and its signal was detected separately. The  
673 detection ranges were specified as 502 nm - 546 nm for eGFP, 662 nm - 732 nm for chlorophyll  
674 and 597 nm - 636 nm for MitoTracker™. The images were acquired as z-stacks with the number  
675 of optical sections varying with the protoplast size. The voxel sizes of the resulting z-stacks were  
676 0.0903, 0.0903, 0.239 µm in the x-y-z order. For visual representation and analysis, single slices  
677 with the best signal-to-noise ratio were selected and extracted from each z-stack using FIJI  
678 software.

## 679 Cultivation of Arabidopsis

680 Seeds were surface-sterilized for 4 min. in 80% ethanol and subsequently for 1 min. in 100%  
681 ethanol. Seeds were placed on plates containing ½ MS supplemented with 1% (D+) sucrose and  
682 0.8% Agar. Alternatively, seeds were directly placed on sterilized soil. Seeds were incubated at  
683 8°C for 2-4 days in the dark for stratification before placing them in growth chambers. Plants were  
684 further cultivated under short day conditions at 22°C and 70 µmol photons/m<sup>2</sup>s in an 8h/16h  
685 light/dark cycle. For bolting assays, plants were placed in a phyto-chamber at 22°C and 70 µmol  
686 photons/m<sup>2</sup>s in a 16h/8h light/dark cycle (long day condition). Rosette leaves and days since  
687 sowing were counted upon appearance of the shoot in the middle of the rosette.

## 688 Screening of Arabidopsis AARE mutants

689 *Arabidopsis thaliana* lines with T-DNA insertions in the At4G14570 locus were identified from the  
690 public T-DNA Express database at the SIGnAL website (Salk Institute Genomic Analysis  
691 Laboratory). Lines GK-456A10, SALK\_080653C, SALK\_071125C, and SALK\_205137C, were  
692 obtained from the Nottingham Arabidopsis Stock Centre. Homozygous mutant alleles were  
693 verified by PCR using the following primers: forward LB GK 5'-  
694 ATATTGACCATCATACTCATTGC-3' and reverse GK-456 5'-CTTCAAAGAAACACCAATCAG-  
695 3' for the GK-456A10 line, and forward LB-pROK 5'-GCGTGGACCGCTTGCTGCAACT-3' and

696 reverse Salk\_53 5'-TCTTTAGCCGAATCAGTTCCAGA-3' for the SALK\_080653C,  
697 SALK\_071125C, and SALK\_205137C lines. Identified homozygous mutant plants were back-  
698 crossed with Arabidopsis Col-0. The F2 generation was screened for homozygous mutant plants  
699 using the above listed primer-sets to identify the mutant allele or substituting the forward primers  
700 with forward WT-GK-456 5'-AAGATGCTTTGCAGTCTCTA-3' and forward WT-Salk 5'-  
701 ACTGCCTTATGATCCATTGTCTC-3', to identify the GK and SALK lines WT alleles, respectively.  
702 RT-PCR was additionally performed to check for the presence of AtAARE transcripts using Taq  
703 polymerase on cDNA prepared as described above with primers At1-At4. All primer combinations  
704 are listed in Supplementary Table S4.

#### 705 AARE exopeptidase activity

706 The enzyme activity assay according to <sup>17</sup> was modified. Here, tissue (80-100 mg) was  
707 homogenized in liquid nitrogen and dissolved in 1 mL extraction buffer (50 mM PBS, 1 mM EDTA,  
708 2 mM DTT). After centrifugation at 20,000 x g for 20 min at 4°C, 300 µL supernatant was mixed  
709 with 700 µL reaction buffer (50 mM HEPES-KOH, pH 7.5 containing 1 mM Ac-Ala-pNA (Bachem,  
710 Bubendorf, Switzerland) or 50 mM HEPES-KOH, pH 7.5, 10% DMSO containing 1mM AcLeu-  
711 pNA (Bachem) and incubated at 37°C for 30-120 min. The reaction was stopped by the addition  
712 of 500 µL 30% acetic acid. Absorbance was measured at 410 nm in a photospectrometer. This  
713 approach was used to generate the data of Fig. 3b and Fig. S6a-d. Later the method was modified  
714 (Fig. 3g, Fig. S6e-g). Here, tissue was homogenized in liquid nitrogen and dissolved in 100 µL  
715 extraction buffer (50 mM PBS, 1 mM EDTA, 2 mM DTT) per 10 mg FW. After centrifugation at  
716 20,000 x g for 20 min at 4°C, 5 µL supernatant was mixed with 195 µL reaction buffer (50 mM  
717 HEPES-KOH, pH 7.5 containing 1 mM Ac-Ala-pNA (Bachem, Bubendorf, Switzerland)) in a 96  
718 well micro titer plate and incubated at 37°C for 30-120 min. In the case of Ac-Leu-pNA as  
719 substrate, 50 mM HEPES-KOH, pH 7.5 with 10% DMSO containing 1mM AcLeu-pNA (Bachem)  
720 was used as reaction buffer. Every biological sample was measured in three technical replicates.  
721 Absorbance was measured at 410 nm. Activity was calculated using a molar absorbance  
722 coefficient<sup>21</sup> of 8.8 mM\*cm<sup>-1</sup> and represents the release of pNA [µmol] per minute normalized to  
723 the total protein concentration of the sample. The protein concentration was determined using the  
724 A<sub>280</sub> method of a NanoDrop™ (Thermo Fisher Scientific) or with a Bradford assay<sup>135</sup>.

#### 725 Western Blots

726 Western Blots were performed as described<sup>74</sup> using the *ECL Advance detection kit* (GE  
727 Healthcare). The primary antibody against *A. thaliana* AARE was kindly provided by Dr. Yasuo



728 Yamauchi<sup>17</sup>. The primary antibody was diluted 1:10,000 in TBST-Buffer with 2% Blocking (GE  
729 Healthcare) and incubated on the membrane for 2 h. As secondary antibody anti-Guinea pig  
730 antibody, coupled to a horseradish peroxidase (Agrisera, AS 10 1496) diluted 1:10,000 in 2%  
731 TBST with 2% Blocking (GE Healthcare), was applied for 1 h.

#### 732 Detection of oxidized proteins

733 Plant tissues were homogenized in liquid nitrogen and proteins were extracted in 50 mM PBS, 50  
734 mM DTT, 1 mM EDTA. 3-6 µg total protein was derivatized with DNPH and subsequently detected  
735 with an anti-DNP antibody according to the manufacturer's instruction of the *OxyBlot Protein*  
736 *Oxidation Detection Kit* (S7150, Sigma-Aldrich). Equal amounts of the derivatized protein samples  
737 were employed as loading control on a separate SDS-gel and stained with Coomassie or silver  
738 staining.

#### 739 Flow cytometry

740 Flow cytometry analysis was performed as described<sup>79</sup>. Here, protonemata were chopped with a  
741 razor blade in a small petri dish (6 cm diameter) in 2 mL of DAPI-buffer containing 0.01 mg/L 4',6-  
742 Diamidin-2-phenylindol (DAPI), 1.07 g/L MgCl<sub>2</sub> x 6 H<sub>2</sub>O, 5 g/L NaCl, 21.11g/L Tris, 0.1% Triton,  
743 pH 7. The solution was filtered using 30 µm pore size filters and the fluorescence intensity was  
744 measured using a Cyflow<sup>®</sup>Space flow cytometry system (Partec, Munich, Germany).

#### 745 Computational predictions

746 Predictions for the presence of cleavable targeting peptides were performed with *TargetP2.0*<sup>63</sup>.  
747 Additional predictions of subcellular localizations were performed with *LOCALIZER*<sup>64</sup>. The  
748 presence of peroxisomal targeting signals was predicted with *PredPlantPTS1*<sup>66,67</sup>. Prediction of  
749 protein domains was performed using *InterProScan*<sup>135</sup> and protein domain annotations according  
750 to PFAM<sup>137</sup> were used.

#### 751 Co-Immunoprecipitation

752 Co-immunoprecipitation was performed using GFP-Trap Magnetic Particles M-270 (Chromotek,  
753 Planegg-Martinsried, Germany) as recommended by the manufacturer with modifications. 300  
754 mg protonema was homogenized in a 2 mL reaction tube using a tungsten and a glass bead. For  
755 each line three biological replicates were realized. The extraction buffer was chosen according to  
756 the manufacturer's recommendations for plant samples and contained 25 mM HEPES-KOH,  
757 pH7.5, 2 mM EDTA, 100 mM NaCl, 200 nM DTT, 0.5% Triton X-100, 1% plant protease inhibitor  
758 cocktail (PPI, P9599, Sigma Aldrich). Ground plant material was dissolved in a final volume of 2

759 mL ice-cold extraction buffer and incubated for 10 min in a water quench ultrasonic device.  
760 Samples were centrifuged at 4°C at 20,000xg for 30 min. For each sample 25 µL magnetic particle  
761 slurry was washed with 500 µL extraction buffer. The sample supernatant was transferred to the  
762 cleaned beads and incubated, rotating for 1 h at 6°C. Subsequently, beads were washed with 1  
763 mL extraction buffer without Triton and PPI and again with 500 µL. Beads were then dissolved in  
764 500 µL wash buffer (10 mM Tris-HCl, pH7.5, 150 mM NaCl, 0.5 mM EDTA), transferred to a new  
765 reaction tube and washed again in 500 µL wash buffer. A RapiGest solution (0.2% in 50 mM Tris-  
766 HCl, pH7.5; RapiGest SF Surfactant (Waters, Milford, MA, USA) was mixed 3:1 with 5 mM DTT  
767 in 50 mM Tris-HCl, pH7.5. 30 µL of the resulting mixture was applied to each sample. Samples  
768 were incubated at 95°C for 5 min under continuous shaking. Samples were cooled down to RT  
769 and 5 µL of a trypsin (V5117, P) solution (0.025 µg/µL in 50 mM Tris-HCl, pH 7.5) were added to  
770 each sample. Digestion on the beads was performed for 30 min at 32°C under continuous  
771 shaking. Supernatants were transferred to new reaction tubes and the remaining beads were  
772 washed twice with 50 µL 5 mM Iodoacetamide solution (in 50 mM Tris-HCl, pH7.5). The wash  
773 supernatants were combined with the trypsin-containing supernatant and incubated over night at  
774 30°C under continuous shaking. Acid-catalysed cleavage of the RapiGest surfactant was  
775 performed as recommended by the manufacturer. Samples were purified using C18-STAGE-Tips  
776 as described<sup>138</sup> and eluted from the Tip in 30% ACN in 0.1% FA.

#### 777 Mass spectrometry measurement and data analysis

778 MS analysis was performed on an Orbitrap Q-Exactive Plus instrument (Thermo Fisher Scientific)  
779 coupled to an UltiMate 3000 RSLCnano system (Dionex LC Packings/Thermo Fisher Scientific)  
780 as described<sup>139</sup>. Database search and label-free quantitation was performed using *MaxQuant*  
781 software V 1.6.0.16<sup>36140</sup>. For each Co-IP a specific database was employed containing all V3.3  
782 proteins of *Physcomitrella*<sup>39</sup> as well as the sequence of the respective fusion protein. Additionally,  
783 the contaminant list provided by the software was included. Decoys were generated on the fly by  
784 reverting the given protein sequences. Variable modifications were formation of pyro Glu (N term  
785 Q, -17.026549 Da), oxidation (M, +15.994915 Da), acetylation (N-term, +42.010565 Da) and  
786 deamidation (N, +0.9 84016 Da). Carbamidomethylation (C, +57. 021464 Da) was specified as  
787 fixed modification. Enzymatic specificity was set to tryptic with semi-specific free N-terminus. An  
788 FDR of 0.01 was set for protein identification. LFQ values<sup>141</sup> were used as quantitative values.  
789 Interaction analysis was performed in Perseus V 1.6.12.0<sup>142</sup>. Missing values were imputed from  
790 a normal distribution with a down-shift of 1.8 and distribution width of 0.3. Interaction partners  
791 were accepted at an FDR of 0.01 and a p-value less than 0.01.

792 Raw files of the test-IP measurements (Fig. S8e) were processed using Mascot Distiller V2.7.10  
793 and searched against all *Physcomitrella* protein models V3.3<sup>39</sup> using Mascot Server V2.7.0  
794 (Matrix Science). Processed mgf files from immunoprecipitation experiments targeting N-terminal  
795 arginylation (PXD003232<sup>36,143</sup>) and the test-IPs were searched again against all *Physcomitrella*  
796 protein models V3.3<sup>39</sup> using Mascot Server V2.7.0 (Matrix Science). The precursor mass  
797 tolerance was 5 ppm and the fragment mass tolerance was 0.02 Da. Variable modifications were  
798 formation of pyro Glu (N term Q, -17.026549 Da), oxidation (M, +15.994915 Da), acetylation (N-  
799 term, +42.010565 Da) and deamidation (N, +0.984016 Da). Carbamidomethylation (C, +57.  
800 021464 Da) was specified as fixed modification. Enzymatic specificity was set to tryptic with semi-  
801 specific free N-terminus. Search results were loaded in Scaffold<sup>TM</sup> 5 (V5.0.1, Proteome Software)  
802 and proteins were accepted at an FDR = 1 and peptides at an FDR = 0.5. A table of identified  
803 proteins is accessible in Supplementary Table S7.

#### 804 Multiple sequence alignment and phylogenetic reconstruction

805 Homologous protein sequences were aligned with UPP<sup>144</sup> (version 4.4.0) using default  
806 parameters and subsequently translated into a codon-aware CDS alignment with PAL2NAL<sup>145</sup>  
807 (version 1.4). Based on this multiple coding sequence alignment we reconstructed a maximum  
808 likelihood tree with RAxML<sup>146</sup> (version 8.2.12) using the GTRCAT model with 1000 rapid bootstrap  
809 samples. The tree was rooted at the split between animal and plant sequences and plotted in R<sup>147</sup>  
810 using the packages ape<sup>148</sup> and ggtree<sup>149</sup>.

#### 811 Statistics and reproducibility

812 Statistical differences in datasets were analysed with one-way Anova with subsequent post-hoc  
813 test if different lines at same conditions were compared. Two-way Anova with subsequent post-  
814 hoc test was performed to analyse differences between lines at different conditions. Sample sizes  
815 of biological replicates are specified in the figure legends. Anova and post-hoc analysis was  
816 performed in R<sup>147</sup>. Statistical significance was accepted at  $p < 0.05$  (\*),  $p < 0.01$  (\*\*) and  $p < 0.001$   
817 (\*\*\*).

#### 818 **Data availability**

819 The authors confirm that all relevant data supporting the findings of this study are available within  
820 the paper and its supplementary files. The mass spectrometry proteomics data have been  
821 deposited at the ProteomeXchange Consortium via the PRIDE partner repository<sup>84,85</sup> with the  
822 dataset identifier PXD033854 and 10.6019/PXD038742. Plant lines used in this study are

823 available upon reasonable request from the corresponding author (R.R.) or *via* the International  
824 Moss Stock Center (IMSC, [www.moss-stock-center.org](http://www.moss-stock-center.org)). IMSC accessions are listed in  
825 Supplementary Table S4. Full Blot images for Fig. 6b and Fig. S3b are available in Fig. S10.  
826 Supplementary Table S8 contains all numeric source data used to generate the graphs and charts  
827 in this study. Plasmids generated in this study are available from the International Moss Stock  
828 Center IMSC (<https://www.moss-stock-center.org>) with the accession numbers P1519 (*PpAARE1*  
829 KO), P1841 (*PpAARE2* KO (pJet)), P1520 (*PpAARE3* KO (pJet)), P1655 (*PpAARE1:Citrine* KI  
830 (pJet)), P1813 (*PpAARE2:Citrine* KI (pJet)), P1814 (*PpAARE3:Citrine* KI), P1833  
831 (*PpAARE1\_1:eGFP* (pMAV4)), P1834 (*PpAARE1\_2:eGFP* (pMAV4)), P1853  
832 (*PpAARE1\_Nt:eGFP* (pMAV4)), P1855 (*PpAARE3:eGFP* (pMAV4)), P1856 (*PpAARE3:eGFP*  
833 (pMAV4)), P1854 (*AtAARE\_SV:eGFP* (pMAV4)), P1881 (*AtAARE\_LV:eGFP* (pMAV4)) and  
834 P1862 (*AtAARE\_Nt:eGFP* (pMAV4)).

### 835 **Acknowledgements**

836 We thank Christine Glockner, Agnes Novakovic and Eija Schulze for expert technical assistance  
837 and Anne Katrin Prowse for language editing. Support with the Arabidopsis assays from Dr.  
838 Philipp Schwenk is gratefully acknowledged. We thank Prof. Dr. Bettina Warscheid for the  
839 possibility to use the QExactive Plus instrument and Prof. Dr. Yasuo Yamauchi for the primary  
840 antibody against *A. thaliana* AARE. We gratefully acknowledge funding by the Deutsche  
841 Forschungsgemeinschaft (DFG, German Research Foundation) under Germany's Excellence  
842 Strategy EXC-2189 (CIBSS to R.R.) and by the Wissenschaftliche Gesellschaft Freiburg. Open  
843 Access funding enabled and organized by Projekt DEAL.

### 844 **Author contributions**

845 S.N.W.H. designed research, performed experiments, analysed data, and wrote the manuscript.  
846 B.Ö. and N.v.G. analysed data and helped writing the manuscript. A.A.M. analysed data. B.R.v.B.,  
847 L.N., J.S.F., R.K., S.G., T.W., and F.S. performed experiments. M.R.F. and S.J.M.S. designed  
848 research and helped writing the manuscript. R.R. designed and supervised research, acquired  
849 funding, and wrote the manuscript. All authors approved the final version of the manuscript.

### 850 **Competing interests**

851 All authors declare to have no competing interests.

852

853 **References**

- 854 1. Mittler, R., Zandalinas, S. I., Fichman, Y. & Van Breusegem, F. Reactive oxygen species  
855 signalling in plant stress responses. *Nature Reviews Molecular Cell Biology* **23**, 663-679  
856 (2022).
- 857 2. Tola, A. J., Jaballi, A. & Missihoun, T. D. Protein carbonylation: Emerging roles in plant  
858 redox biology and future prospects. *Plants* **10**, 1451 (2021).
- 859 3. Gratão, P. L., Polle, A., Lea, P. J. & Azevedo, R. A. Making the life of heavy metal-stressed  
860 plants a little easier. *Functional Plant Biology* **32**, 481-494 (2005).
- 861 4. Smirnoff, N. Ascorbic acid: metabolism and functions of a multi-faceted molecule. *Current*  
862 *Opinion in Plant Biology* **3**, 229-235 (2000).
- 863 5. Sharma, P., Jha, A. B., Dubey, R. S. & Pessarakli, M. Reactive oxygen species, oxidative  
864 damage, and antioxidative defense mechanism in plants under stressful conditions.  
865 *Journal of Botany* **2012**: 217037 (2012).
- 866 6. Müller-Schüssele, S. J., et al. Chloroplasts require glutathione reductase to balance  
867 reactive oxygen species and maintain efficient photosynthesis. *Plant Journal* **103**, 1140-  
868 1154 (2020).
- 869 7. Soares, C., Carvalho, M. E., Azevedo, R. A. & Fidalgo, F. Plants facing oxidative  
870 challenges—A little help from the antioxidant networks. *Environmental and Experimental*  
871 *Botany* **161**, 4-25 (2019)
- 872 8. Parsell, D. A., Kowal, A. S., Singer, M. A. & Lindquist, S. Protein disaggregation mediated  
873 by heat-shock protein Hsp104. *Nature* **372**, 475-478 (1994).
- 874 9. Queitsch, C., Hong, S. W., Vierling, E. & Lindquist, S. Heat shock protein 101 plays a  
875 crucial role in thermotolerance in Arabidopsis. *Plant Cell* **12**, 479-492 (2000).
- 876 10. Mogk, A., Bukau, B. & Kampinga, H. H. Cellular handling of protein aggregates by  
877 disaggregation machines. *Molecular Cell* **69**, 214-226 (2018).
- 878 11. Møller, I. M., Jensen, P. E. & Hansson, A. Oxidative modifications to cellular components  
879 in plants. *Annual Review of Plant Biology* **58**, 459-481 (2007).
- 880 12. Ciacka, K., Tymiński, M., Gniazdowska, A. & Krasuska, U. Carbonylation of proteins—an  
881 element of plant ageing. *Planta* **252**, 12 (2020).
- 882 13. Farooq, M. A., et al. Acquiring control: The evolution of ROS-Induced oxidative stress and  
883 redox signaling pathways in plant stress responses. *Plant Physiology and Biochemistry*  
884 **141**, 353-369 (2019).
- 885 14. Bartlam, M., et al. Crystal structure of an acylpeptide hydrolase/esterase from *Aeropyrum*  
886 *pernix K1*. *Structure* **12**, 1481-1488 (2004).

- 887 15. Brunialti, E. A., Gatti-Lafranconi, P. & Lotti, M. Promiscuity, stability and cold adaptation  
888 of a newly isolated acylaminoacyl peptidase. *Biochimie* **93**, 1543-1554 (2011).
- 889 16. Tsunasawa, S., Narita, K. & Ogata, K. Purification and properties of acylamino acid-  
890 releasing enzyme from rat liver. *Journal of Biochemistry* **77**, 89-102 (1975).
- 891 17. Yamauchi, Y., Ejiri, Y., Toyoda, Y. & Tanaka, K. Identification and biochemical  
892 characterization of plant acylamino acid-releasing enzyme. *Journal of Biochemistry* **134**,  
893 251-257 (2003).
- 894 18. Rawlings, N. D., et al. The MEROPS database of proteolytic enzymes, their substrates  
895 and inhibitors in 2017 and a comparison with peptidases in the PANTHER database.  
896 *Nucleic Acids Research* **46**, D624-D632 (2018).
- 897 19. Fujino, T., et al. Identification of the cleavage sites of oxidized protein that are susceptible  
898 to oxidized protein hydrolase (OPH) in the primary and tertiary structures of the protein.  
899 *Journal of Biochemistry* **127**, 1087-1093 (2000).
- 900 20. Shimizu, K., et al. Overexpression of oxidized protein hydrolase protects COS-7 cells from  
901 oxidative stress-induced inhibition of cell growth and survival. *Biochemical and Biophysical*  
902 *Research Communications* **304**, 766-771 (2003).
- 903 21. Nakai, A., Yamauchi, Y., Sumi, S. & Tanaka, K. Role of acylamino acid-releasing  
904 enzyme/oxidized protein hydrolase in sustaining homeostasis of the cytoplasmic  
905 antioxidative system. *Planta* **236**, 427-436 (2012).
- 906 22. Gogliettino, M., et al. A novel class of bifunctional acylpeptide hydrolases-potential role in  
907 the antioxidant defense systems of the Antarctic fish *Trematomus bernacchii*. *FEBS*  
908 *Journal* **281**, 401-415 (2014).
- 909 23. Kiss, A. L., et al. The acylaminoacyl peptidase from *Aeropyrum pernix* K1 thought to be  
910 an exopeptidase displays endopeptidase activity. *Journal of Molecular Biology* **368**, 509-  
911 520 (2007).
- 912 24. Szeltner, Z., et al. Characterization of a novel acylaminoacyl peptidase with hexameric  
913 structure and endopeptidase activity. *Biochimica et Biophysica Acta (BBA)-Proteins and*  
914 *Proteomics* **1794**, 1204-1210 (2009).
- 915 25. Gogliettino, M., et al. Identification and characterisation of a novel acylpeptide hydrolase  
916 from *Sulfolobus solfataricus*: structural and functional insights. *PLOS ONE* **7**, e37921  
917 (2012).
- 918 26. Scaloni, A., et al. Deficiency of acylpeptide hydrolase in small-cell lung carcinoma cell  
919 lines. *Journal of Laboratory and Clinical Medicine* **120**, 546-552 (1992).

- 920 27. Riccio, A., et al. A new APEH cluster with antioxidant functions in the antarctic  
921 hemoglobinless icefish *Chionodraco hamatus*. *PLOS ONE* **10**, e0125594 (2015).
- 922 28. Gogliettino, M., et al. Selective inhibition of acylpeptide hydrolase in SAOS-2  
923 osteosarcoma cells: is this enzyme a viable anticancer target? *Molecular Biology Reports*  
924 **48**, 1505-1519 (2021).
- 925 29. Tangri, A., et al. Deubiquitinase UCHL1 maintains protein homeostasis through the  
926 PSMA7–APEH–Proteasome axis in high-grade serous ovarian carcinoma. *Molecular*  
927 *Cancer Research* **19**, 1168-1181 (2021).
- 928 30. Palumbo, R., et al. APEH inhibition affects osteosarcoma cell viability via downregulation  
929 of the proteasome. *International Journal of Molecular Sciences* **17**, 1614 (2016).
- 930 31. Shimizu, K., Kiuchi, Y., Ando, K., Hayakawa, M. & Kikugawa, K. Coordination of oxidized  
931 protein hydrolase and the proteasome in the clearance of cytotoxic denatured proteins.  
932 *Biochemical and Biophysical Research Communications* **324**, 140–146 (2004).
- 933 32. Palmieri, G., et al. Acylpeptide hydrolase inhibition as targeted strategy to induce  
934 proteasomal down-regulation. *PLOS ONE* **6**, e25888 (2011).
- 935 33. Bergamo, P., et al. RedOx status, proteasome and APEH: Insights into anticancer  
936 mechanisms of t10, c12-conjugated linoleic acid isomer on A375 melanoma cells. *PLOS*  
937 *ONE* **8**, e80900 (2013).
- 938 34. Yamin, R., Zhao, C., O'Connor, P. B., McKee, A. C. & Abraham, C. R. Acyl peptide  
939 hydrolase degrades monomeric and oligomeric amyloid-beta peptide. *Molecular*  
940 *Neurodegeneration* **4**, 33 (2009).
- 941 35. Bachovchin, D. A., et al. A high-throughput, multiplexed assay for superfamily-wide  
942 profiling of enzyme activity. *Nature Chemical Biology* **10**, 656-663 (2014).
- 943 36. Hoernstein, S. N. W., et al. Identification of targets and interaction partners of arginyl-tRNA  
944 protein transferase in the moss *Physcomitrella patens*. *Molecular & Cellular Proteomics*  
945 **15**, 1808-1822 (2016).
- 946 37. Schuessele, C., et al. Spatio-temporal patterning of arginyl-tRNA protein transferase  
947 (ATE) contributes to gametophytic development in a moss. *New Phytologist* **209**, 1014–  
948 1027 (2016).
- 949 38. Varshavsky, A. N-degron and C-degron pathways of protein degradation. *Proceedings of*  
950 *the National Academy of Sciences U.S.A.* **116**, 358-366 (2019).
- 951 39. Lang, D., et al. The *Physcomitrella patens* chromosome-scale assembly reveals moss  
952 genome structure and evolution. *Plant Journal* **93**, 515-533 (2018).

- 953 40. Chen, F., Mackey, A. J., Stoeckert Jr, C. J. & Roos DS OrthoMCL-DB: querying a  
954 comprehensive multi-species collection of ortholog groups. *Nucleic Acids Research* **34**,  
955 D363-D368 (2006).
- 956 41. Zimmer, A. D., et al. Reannotation and extended community resources for the genome of  
957 the non-seed plant *Physcomitrella patens* provide insights into the evolution of plant gene  
958 structures and functions. *BMC Genomics* **14**, 498 (2013).
- 959 42. Fernandez-Pozo, N., et al. PEATmoss (Physcomitrella Expression Atlas Tool): a unified  
960 gene expression atlas for the model plant *Physcomitrella patens*. *Plant Journal* **102**, 165-  
961 177 (2020).
- 962 43. Mergner, J., et al. Mass-spectrometry-based draft of the *Arabidopsis* proteome. *Nature*  
963 **579**, 409-414 (2020).
- 964 44. Altschul, S. F., et al. Gapped BLAST and PSI-BLAST: a new generation of protein  
965 database search programs. *Nucleic Acids Research* **25**, 3389-3402 (1997).
- 966 45. Merchant, S. S., et al. The *Chlamydomonas* genome reveals the evolution of key animal  
967 and plant functions. *Science* **318**, 245-250 (2007).
- 968 46. Bowman, J. L., et al. Insights into land plant evolution garnered from the *Marchantia*  
969 *polymorpha* genome. *Cell* **171**, 287-304 (2017).
- 970 47. Banks, J. A., et al. The *Selaginella* genome identifies genetic changes associated with the  
971 evolution of vascular plants. *Science* **332**, 960-963 (2011).
- 972 48. Ouyang, S., et al. The TIGR rice genome annotation resource: improvements and new  
973 features. *Nucleic Acids Research* **35**, D883-D887 (2007).
- 974 49. Tuskan, G. A., et al. The genome of black cottonwood, *Populus trichocarpa* (Torr. & Gray).  
975 *Science* **313**, 1596-1604 (2006).
- 976 50. Hori, K., et al. *Klebsormidium flaccidum* genome reveals primary factors for plant terrestrial  
977 adaptation. *Nature Communications* **5**, 3978 (2014).
- 978 51. Kirbis, A., et al. Transcriptional landscapes of divergent sporophyte development in two  
979 mosses, *Physcomitrium* (*Physcomitrella*) *patens* and *Funaria hygrometrica*. *Frontiers in*  
980 *Plant Science* **11**, 747 (2020).
- 981 52. Ostendorf, A. K., et al. Polyploidization within the Funariaceae – a key principle behind  
982 speciation, sporophyte reduction and the high variance of spore diameters? *Bryophyte*  
983 *Diversity and Evolution* **43**, 164-179 (2021).
- 984 53. Lamesch, P., et al. The Arabidopsis Information Resource (TAIR): improved gene  
985 annotation and new tools. *Nucleic Acids Research* **40**, D1202-D1210 (2012).



- 986 54. Rawlings, N. D., Polgar, L. & Barrett, A. J. A new family of serine-type peptidases related  
987 to prolyl oligopeptidase. *Biochemical Journal* **279**, 907-908 (1991).
- 988 55. Polgar, L. The prolyl oligopeptidase family. *Cellular and Molecular Life Sciences* **59**, 349-  
989 362 (2002).
- 990 56. Perroud, P. F., et al. The *Physcomitrella patens* gene atlas project: large-scale RNA-seq  
991 based expression data. *Plant Journal* **95**, 168-182 (2018).
- 992 57. Mueller, S. J., et al. Quantitative analysis of the mitochondrial and plastid proteomes of  
993 the moss *Physcomitrella patens* reveals protein macrocompartmentation and  
994 microcompartmentation. *Plant Physiology* **164**, 2081-2095 (2014).
- 995 58. Fesenko, I. A., et al. Specific pools of endogenous peptides are present in gametophore,  
996 protonema, and protoplast cells of the moss *Physcomitrella patens*. *BMC Plant Biology*  
997 **15**, 87 (2015).
- 998 59. Fesenko, I., et al. The *Physcomitrella patens* chloroplast proteome changes in response  
999 to protoplastation. *Frontiers in Plant Science* **7**, 1661 (2016).
- 1000 60. Liu, H., et al. The emergence and evolution of intron-poor and intronless genes in intron-  
1001 rich plant gene families. *Plant Journal* **105**, 1072-1082 (2021).
- 1002 61. Beike, A. K. et al. Insights from the cold transcriptome of *Physcomitrella patens*: global  
1003 specialization pattern of conserved transcriptional regulators and identification of orphan  
1004 genes involved in cold acclimation. *New Phytologist* **205**, 869-881 (2015).
- 1005 62. Cheng, C. Y., et al. Araport11: a complete reannotation of the *Arabidopsis thaliana*  
1006 reference genome. *Plant Journal* **89**, 789-804 (2017).
- 1007 63. Armenteros, J. J. A., et al. Detecting sequence signals in targeting peptides using deep  
1008 learning. *Life Science Alliance* **2**, e201900429 (2019).
- 1009 64. Sperschneider, J., et al. LOCALIZER: subcellular localization prediction of both plant and  
1010 effector proteins in the plant cell. *Scientific Reports* **7**, 44598 (2017).
- 1011 65. Waszczak, C., Carmody, M. & Kangasjärvi, J. Reactive oxygen species in plant signaling.  
1012 *Annual Review of Plant Biology* **69**, 209-236 (2018).
- 1013 66. Lingner, T., et al. Identification of novel plant peroxisomal targeting signals by a  
1014 combination of machine learning methods and *in vivo* subcellular targeting analyses. *Plant*  
1015 *Cell* **23**, 1556-1572 (2011).
- 1016 67. Reumann, S., Buchwald, D. & Lingner, T. PredPlantPTS1: a web server for the prediction  
1017 of plant peroxisomal proteins. *Frontiers in Plant Science* **3**, 194 (2012).
- 1018 68. Gould, S. J., Keller, G. A., Hosken, N., Wilkinson, J. & Subramani, S. A conserved  
1019 tripeptide sorts proteins to peroxisomes. *Journal of Cell Biology* **108**, 1657-1664 (1989).

- 1020 69. Wang, J., Wang, Y., Gao, C., Jiang, L. & Guo, D. PPero, a computational model for plant  
1021 PTS1 type peroxisomal protein prediction. *PLOS ONE* **12**, e0168912 (2017).
- 1022 70. Petriv, I., Tang, L., Titorenko, V. I. & Rachubinski, R. A. A new definition for the consensus  
1023 sequence of the peroxisome targeting signal type 2. *Journal of Molecular Biology* **341**,  
1024 119-134 (2004).
- 1025 71. Reumann, S. Specification of the peroxisome targeting signals type 1 and type 2 of plant  
1026 peroxisomes by bioinformatics analyses. *Plant Physiology* **135**, 783-800 (2004).
- 1027 72. Weise, A., et al. Use of *Physcomitrella patens actin* 5' regions for high transgene  
1028 expression: importance of 5' introns. *Applied Microbiology and Biotechnology* **70**, 337-345  
1029 (2006).
- 1030 73. Özdemir, B., et al. Cytological analysis and structural quantification of FtsZ1-2 and FtsZ2-  
1031 1 network characteristics in *Physcomitrella patens*. *Scientific Reports* **8**, 11165 (2018).
- 1032 74. Lang, E. G. E., et al. Simultaneous isolation of pure and intact chloroplasts and  
1033 mitochondria from moss as the basis for sub-cellular proteomics. *Plant Cell Reports* **30**,  
1034 205–215 (2011).
- 1035 75. Fuss, J., Liegmann, O., Krause, K. & Rensing, S. A. Green targeting predictor and  
1036 ambiguous targeting predictor 2: the pitfalls of plant protein targeting prediction and of  
1037 transient protein expression in heterologous systems. *New Phytologist* **200**, 1022-1033  
1038 (2013).
- 1039 76. Orr, M. W., Mao, Y., Storz, G. & Qian, S. B. Alternative ORFs and small ORFs: shedding  
1040 light on the dark proteome. *Nucleic Acids Research* **48**, 1029-1042 (2020).
- 1041 77. Hohe, A., et al. An improved and highly standardised transformation procedure allows  
1042 efficient production of single and multiple targeted gene-knockouts in a moss,  
1043 *Physcomitrella patens*. *Current Genetics* **44**, 339-347 (2004).
- 1044 78. Noy-Malka, et al. A single CMT methyltransferase homolog is involved in CHG DNA  
1045 methylation and development of *Physcomitrella patens*. *Plant Molecular Biology* **84**, 719-  
1046 735 (2014).
- 1047 79. Heck, M. A., et al. Axenic *in vitro* cultivation of 19 peat moss (*Sphagnum* L.) species as a  
1048 resource for basic biology, biotechnology, and paludiculture. *New Phytologist* **229**, 861-  
1049 876 (2021).
- 1050 80. Kamisugi, Y., et al. The mechanism of gene targeting in *Physcomitrella patens*:  
1051 homologous recombination, concatenation and multiple integration. *Nucleic Acids*  
1052 *Research* **34**, 6205-6214 (2006).

- 1053 81. Rempfer, C., et al. Autopolyploidization affects transcript patterns and gene targeting  
1054 frequencies in *Physcomitrella*. *Plant Cell Reports* **41**, 153-173 (2022).
- 1055 82. Lorenz, S., Tintelnot, S., Reski, R. & Decker, E. L. Cyclin D-knockout uncouples  
1056 developmental progression from sugar availability. *Plant Molecular Biology* **53**, 227-236  
1057 (2003).
- 1058 83. Dalle-Donne, I., et al. Protein carbonylation: 2, 4-dinitrophenylhydrazine reacts with both  
1059 aldehydes/ketones and sulfenic acids. *Free Radical Biology and Medicine* **46**, 1411-1419  
1060 (2009).
- 1061 84. Deutsch, E. W., et al. The ProteomeXchange consortium in 2020: enabling 'big data'  
1062 approaches in proteomics. *Nucleic Acids Research* **48**, D1145-D1152 (2020).
- 1063 85. Perez-Riverol, Y., et al. The PRIDE database resources in 2022: a hub for mass  
1064 spectrometry-based proteomics evidences. *Nucleic Acids Research* **50**, D543-D552  
1065 (2022).
- 1066 86. Johansson, E., Olsson, O. & Nyström, T. Progression and specificity of protein oxidation  
1067 in the life cycle of *Arabidopsis thaliana*. *Journal of Biological Chemistry* **279**, 22204-22208  
1068 (2004).
- 1069 87. Harman, D. Aging: A theory based on free radical and radiation chemistry. *Journal of*  
1070 *Gerontology* **11**, 298–300 (1956).
- 1071 88. Harman, D. The biologic clock: the mitochondria? *Journal of the American Geriatrics*  
1072 *Society* **20**, 145-147 (1972).
- 1073 89. Giorgi, C., et al. Mitochondria and reactive oxygen species in aging and age-related  
1074 diseases. *International Review of Cell and Molecular Biology* **340**, 209-344 (2018).
- 1075 90. Mao, C., et al. Nitric oxide regulates seedling growth and mitochondrial responses in aged  
1076 oat seeds. *International Journal of Molecular Sciences* **19**, 1052 (2018).
- 1077 91. Ratajczak, E., Małecka, A., Ciereszko, I. & Staszak, A. M. Mitochondria are important  
1078 determinants of the aging of seeds. *International Journal of Molecular Sciences* **20**, 1568  
1079 (2019).
- 1080 92. Munné-Bosch, S. & Alegre, L. Plant aging increases oxidative stress in chloroplasts.  
1081 *Planta* **214**, 608-615 (2002).
- 1082 93. Noctor, G., Veljovic-Jovanovic, S., Driscoll, S., Novitskaya, L. & Foyer, C. H. Drought and  
1083 oxidative load in the leaves of C3 plants: a predominant role for photorespiration? *Annals*  
1084 *of Botany* **89**, 841-850 (2002).

- 1085 94. Foyer, C. H. & Noctor, G. Redox sensing and signalling associated with reactive oxygen  
1086 in chloroplasts, peroxisomes and mitochondria. *Physiologia Plantarum* **119**, 355-364  
1087 (2003).
- 1088 95. Sohal, R. S. & Weindruch, R. Oxidative stress, caloric restriction, and aging. *Science*, **273**,  
1089 59-63 (1996).
- 1090 96. López-Otín, C., Blasco, M. A., Partridge, L., Serrano, M. & Kroemer, G. The hallmarks of  
1091 aging. *Cell* **153**, 1194-1217 (2013).
- 1092 97. Senthilkumar, R., Reddy, P. N. & Sharma, K. K. Studies on trypsin-modified bovine and  
1093 human lens acylpeptide hydrolase. *Experimental Eye Research* **72**, 301-310 (2001).
- 1094 98. Palmieri, G., et al. Low erythrocyte levels of proteasome and acyl-peptide hydrolase  
1095 (APEH) activities in Alzheimer's disease: a sign of defective proteostasis? *Journal of*  
1096 *Alzheimer's Disease* **60**, 1097-1106 (2017).
- 1097 99. Marshall, I., et al. Analyzing the activity and expression of acyl peptide enzyme hydrolase  
1098 (APEH) in the blood serum of patients with type II diabetes. *Bios* **90**, 70-78 (2019).
- 1099 100. Resemann, H. C., et al. Convergence of sphingolipid desaturation across over 500  
1100 million years of plant evolution. *Nature Plants* **7**, 219-232 (2021).
- 1101 101. Zybaylov, B., et al. Sorting signals, N-terminal modifications, and abundance of the  
1102 chloroplast proteome. *PLOS ONE* **3**, e1994 (2008).
- 1103 102. Rugen, N., et al. Protein interaction patterns in *Arabidopsis thaliana* leaf  
1104 mitochondria change in dependence to light. *Biochimica et Biophysica Acta (BBA)-*  
1105 *Bioenergetics* **1862**, 148443 (2021).
- 1106 103. Maxwell, D. P., Wang, Y. & McIntosh, L. The alternative oxidase lowers  
1107 mitochondrial reactive oxygen production in plant cells. *Proceedings of the National*  
1108 *Academy of Sciences U.S.A.* **96**, 8271-8276 (1999).
- 1109 104. Møller, I. M. Plant mitochondria and oxidative stress: electron transport, NADPH  
1110 turnover, and metabolism of reactive oxygen species. *Annual Review of Plant Biology* **52**,  
1111 561-591 (2001).
- 1112 105. Smakowska, E., Czarna, M. & Janska, H. Mitochondrial ATP-dependent proteases  
1113 in protection against accumulation of carbonylated proteins. *Mitochondrion* **19**, 245-251  
1114 (2014).
- 1115 106. Al-Khatib, K. & Paulsen, G. M. Enhancement of thermal injury to photosynthesis in  
1116 wheat plants and thylakoids by high light intensity. *Plant Physiology* **90**, 1041-1048 (1989).

- 1117 107. Wang, Q. L., Chen, J. H., He, N. Y. & Guo, F. Q. Metabolic reprogramming in  
1118 chloroplasts under heat stress in plants. *International Journal of Molecular Sciences* **19**,  
1119 849 (2018).
- 1120 108. Sweetlove, L. J., et al. The impact of oxidative stress on Arabidopsis mitochondria.  
1121 *Plant Journal* **32**, 891-904 (2002).
- 1122 109. Tiwari, B. S., Belenghi, B. & Levine, A. Oxidative stress increased respiration and  
1123 generation of reactive oxygen species, resulting in ATP depletion, opening of  
1124 mitochondrial permeability transition, and programmed cell death. *Plant Physiology* **128**,  
1125 1271-1281 (2002).
- 1126 110. Willems, P., Ndah, E., Jonckheere, V., van Breusegem, F. & van Damme, P. To  
1127 new beginnings: Riboproteogenomics discovery of N-terminal proteoforms in *Arabidopsis*  
1128 *thaliana*. *Frontiers in Plant Science* **12**, 778804 (2021).
- 1129 111. Kiessling, J., et al. Dual targeting of plastid division protein FtsZ to chloroplasts  
1130 and the cytoplasm. *EMBO Reports* **5**, 889-894 (2004).
- 1131 112. van Wijk, K. J., et al. The Arabidopsis PeptideAtlas: Harnessing worldwide  
1132 proteomics data to create a comprehensive community proteomics resource. *Plant Cell*  
1133 **33**, 3421-3453 (2021).
- 1134 113. Zhang, H., et al. Arabidopsis proteome and the mass spectral assay library.  
1135 *Scientific Data* **6**, 278 (2019).
- 1136 114. Zeng, Z., et al. Acylpeptide hydrolase is a component of the cellular response to  
1137 DNA damage. *DNA Repair* **58**, 52-61 (2017).
- 1138 115. Brocca, S., et al. A bacterial acyl aminoacyl peptidase couples flexibility and  
1139 stability as a result of cold adaptation. *FEBS Journal* **283**, 4310-4324 (2016).
- 1140 116. Menyhárd, D. K., et al. A self-compartmentalizing hexamer serine protease from  
1141 *Pyrococcus horikoshii*: substrate selection achieved through multimerization. *Journal of*  
1142 *Biological Chemistry* **288**, 17884-17894 (2013).
- 1143 117. Viaene, T., et al. Directional auxin transport mechanisms in early diverging land  
1144 plants. *Current Biology* **24**, 2786-2791 (2014).
- 1145 118. Chen, Z., et al. Comprehensive analysis of the *Ppatg3* mutant reveals that  
1146 autophagy plays important roles in gametophore senescence in *Physcomitrella patens*.  
1147 *BMC Plant Biology* **20**, 440 (2020).
- 1148 119. Jia, M., et al. Noncanonical ATG8-ABS3 interaction controls senescence in plants.  
1149 *Nature Plants* **5**, 212-224 (2019).

- 1150 120. Dalle-Donne, I., Giustarini, D., Colombo, R., Rossi, R. & Milzani, A. Protein  
1151 carbonylation in human diseases. *Trends in Molecular Medicine* **9**, 169-176 (2003).
- 1152 121. Hipp, M. S., Kasturi, P. & Hartl, F. U. The proteostasis network and its decline in  
1153 ageing. *Nature Reviews Molecular Cell Biology* **20**, 421-435 (2019).
- 1154 122. Chen, Y. R., et al. Tissue-specific landscape of protein aggregation and quality  
1155 control in an aging vertebrate. Preprint at: <https://doi.org/10.1101/2022.02.26.482120>  
1156 (2022).
- 1157 123. Medina, R., et al. Phylogenomic delineation of *Physcomitrium* (Bryophyta:  
1158 Funariaceae) based on targeted sequencing of nuclear exons and their flanking regions  
1159 rejects the retention of *Physcomitrella*, *Physcomitridium* and *Aphanorrhagma*. *Journal of*  
1160 *Systematics and Evolution* **57**, 404-417 (2019).
- 1161 124. Reski, R. & Abel, W. O. Induction of budding on chloronemata and caulonemata  
1162 of the moss, *Physcomitrella patens*, using isopentenyladenine. *Planta* **165**, 354-358  
1163 (1985).
- 1164 125. Egner, T., et al. High frequency of phenotypic deviations in *Physcomitrella patens*  
1165 plants transformed with a gene-disruption library. *BMC Plant Biology* **2**, 6 (2002).
- 1166 126. Schween, G., Hohe, A., Koprivova, A. & Reski, R. Effects of nutrients, cell density  
1167 and culture techniques on protoplast regeneration and early protonema development in a  
1168 moss, *Physcomitrella patens*. *Journal of Plant Physiology* **160**, 209–212 (2003).
- 1169 127. Erxleben, A., Gessler, A., Vervliet-Scheebaum, M. & Reski, R. Metabolite profiling  
1170 of the moss *Physcomitrella patens* reveals evolutionary conservation of osmoprotective  
1171 substances. *Plant Cell Reports* **31**, 427-436 (2012).
- 1172 128. Tian, G. W., et al. High-throughput fluorescent tagging of full-length *Arabidopsis*  
1173 gene products in planta. *Plant Physiology* **135**, 25-38 (2004).
- 1174 129. Sambrook, J. & Russell, D. W. Standard ethanol precipitation of DNA in  
1175 microcentrifuge tubes. *Cold Spring Harbor Protocols* **2006**, pdb-prot4456 (2006).
- 1176 130. Hohe, A. & Reski, R. Optimisation of a bioreactor culture of the moss  
1177 *Physcomitrella patens* for mass production of protoplasts. *Plant Science* **163**, 69-74  
1178 (2002).
- 1179 131. Decker, E. L., et al. Strigolactone biosynthesis is evolutionarily conserved,  
1180 regulated by phosphate starvation and contributes to resistance against phytopathogenic  
1181 fungi in a moss, *Physcomitrella patens*. *New Phytologist* **216**, 455-468 (2017).
- 1182 132. Gibson, D. G., et al. Enzymatic assembly of DNA molecules up to several hundred  
1183 kilobases. *Nature Methods* **6**, 343–345 (2009).

- 1184 133. Amack, S. C. & Antunes, M. S. CaMV35S promoter—a plant biology and  
1185 biotechnology workhorse in the era of synthetic biology. *Current Plant Biology* **24**, 100179  
1186 (2020).
- 1187 134. Horstmann, V., Huether, C. M., Jost, W., Reski, R. & Decker, E. L. Quantitative  
1188 promoter analysis in *Physcomitrella patens*: a set of plant vectors activating gene  
1189 expression within three orders of magnitude. *BMC Biotechnology* **4**, 13 (2004).
- 1190 135. Bradford, M. M. A rapid and sensitive method for the quantitation of microgram  
1191 quantities of protein utilizing the principle of protein-dye binding. *Analytical Biochemistry*  
1192 **72**, 248-254 (1976).
- 1193 136. Blum, M., et al. The InterPro protein families and domains database: 20 years on.  
1194 *Nucleic Acids Research* **49**, D344-D354 (2021).
- 1195 137. Mistry, J., et al. Pfam: The protein families database in 2021. *Nucleic Acids*  
1196 *Research* **49**, D412-D419 (2021).
- 1197 138. Hoernstein, S. N. W., et al. Host cell proteome of *Physcomitrella patens* harbors  
1198 proteases and protease inhibitors under bioproduction conditions. *Journal of Proteome*  
1199 *Research* **17**, 3749-3760 (2018).
- 1200 139. Top, O., et al. Expression of a human cDNA in moss results in spliced mRNAs and  
1201 fragmentary protein isoforms. *Communications Biology* **4**, 964 (2021).
- 1202 140. Cox, J. & Mann, M. MaxQuant enables high peptide identification rates,  
1203 individualized ppb-range mass accuracies and proteome-wide protein quantification.  
1204 *Nature Biotechnology* **26**, 1367-1372 (2008).
- 1205 141. Cox, J., et al. Accurate proteome-wide label-free quantification by delayed  
1206 normalization and maximal peptide ratio extraction, termed MaxLFQ. *Molecular & Cellular*  
1207 *Proteomics* **13**, 2513-2526 (2014).
- 1208 142. Tyanova, S., et al. The Perseus computational platform for comprehensive  
1209 analysis of (prote)omics data. *Nature Methods* **13**, 731-740 (2016).
- 1210 143. Hoernstein, S. N. W., et al. Identification of targets and interaction partners of  
1211 arginyl-tRNA protein transferase in the moss *Physcomitrella patens*.  
1212 <http://dx.doi.org/10.6019/PXD003232> (2016).
- 1213 144. Nguyen, N. D., Mirarab, S., Kumar, K. & Warnor, T. Ultra-large alignments using  
1214 phylogeny-aware profiles. *Genome Biology* **16**, 124 (2015).
- 1215 145. Suyama, M., Torrents, D. & Bork, P. PAL2NAL: robust conversion of protein  
1216 sequence alignments into the corresponding codon alignments. *Nucleic Acids Research*  
1217 **34**, W609–W612 (2006).

- 1218 146. Stamatakis, A. RAxML version 8: a tool for phylogenetic analysis and post-analysis  
1219 of large phylogenies. *Bioinformatics* **30**, 1312–1313 (2014).
- 1220 147. R Core Team. R: A language and environment for statistical computing. R  
1221 Foundation for Statistical Computing, Vienna, Austria. URL <https://www.R-project.org/>  
1222 (2022).
- 1223 148. Paradis, E. & Schliep, K. ape 5.0: an environment for modern phylogenetics and  
1224 evolutionary analyses in R. *Bioinformatics* **35**, 526-528 (2018).
- 1225 149. Yu, G., Smith, D., Zhu, H., Guan, Y. & Lam, T. T. ggtree: an R package for  
1226 visualization and annotation of phylogenetic trees with their covariates and other  
1227 associated data. *Methods in Ecology and Evolution* **8**, 28-36 (2017).

1228

## 1229 **Supplementary Information**

1230 **Figure S1** Expression levels of PpAARE genes and AtAARE in different tissues and under stress  
1231 conditions.

1232 **Figure S2** Sequence alignment of AtAARE and PtAARE isoforms.

1233 **Figure S3** AARE activity in *Physcomitrella* plastids and mitochondria.

1234 **Figure S4** Identification of PpAARE single, double and triple KO mutants by PCR on genomic  
1235 DNA.

1236 **Figure S5** FCM analysis of all confirmed PpAARE KO lines to analyse the ploidy.

1237 **Figure S6** AARE exopeptidase activity protonema of KO mutants.

1238 **Figure S7** Plate overview and additional OxyBlots from *Physcomitrella* gametophore colonies  
1239 with loading controls.

1240 **Figure S8** Screening for haploid *Physcomitrella* lines with a citrine fusion transcript and overview  
1241 on identification of the three PpAARE isoforms in different IP experiments.

1242 **Figure S9** Phenotypes of seedlings and adult AtAARE T-DNA mutant lines (GK, s68) and WT  
1243 (Col).

1244 **Supplementary Table S1** List of primers used to assemble KO and KI constructs and primers  
1245 used to screen for transgenic plants in *Physcomitrella*.



1246 **Supplementary Table S2** List of gene accession numbers for all sequences used for  
1247 phylogenetic analysis and corresponding subcellular localization predictions.

1248 **Supplementary Table S3** List of primers used to screen possible T-DNA mutant plants in  
1249 Arabidopsis.

1250 **Supplementary Table S4** List of accession numbers for the International Moss Stock Center  
1251 (IMSC) of all transgenic Physcomitrella lines.

1252 **Supplementary Table S5** List of primers used for qPCR on genomic DNA to determine copy  
1253 numbers of KO constructs in transgenic Physcomitrella lines.

1254 **Supplementary Table S6** List of primers used to assemble the constructs for transient  
1255 localization analysis in Physcomitrella protoplasts.

1256 **Supplementary Table S7** Spectrum report of the revised database search of the anti-Arg<sup>(Nt)</sup> IP  
1257 published in<sup>36</sup>.

1258 **Supplementary Table S8** This table contains all numeric source data used to generate the  
1259 graphs in Fig. 3b, Fig. 3e-g, Fig. 5b, Fig. 6c, Fig. 6e, Fig. S1, Fig. S3c, Fig. S4j-p, Fig. S5, Fig.  
1260 S6, Fig. S8d, Fig. S8e and Fig. S8g.

1261

1262 **Fig. 1 Phylogenetic tree for AARE isoforms from selected organisms, gene structures and**  
1263 **proteins domains of *P. patens* and *A. thaliana* AARE isoforms.** (a) Maximum likelihood tree  
1264 based on an alignment of multiple *AARE* coding sequences. Duplication events in several species  
1265 appear to be lineage-specific. Node values reflect percentage confidence values based on 1000  
1266 bootstrap replicates. Species abbreviations: At: *Arabidopsis thaliana*; Pt: *Populus trichocarpa*; Os:  
1267 *Oryza sativa*; Pp: *Physcomitrium patens*; Fh: *Funaria hygrometrica*; Sf: *Sphagnum fallax*; Mp:  
1268 *Marchantia polymorpha*; Sm: *Selaginella moellendorffii*; Kn: *Klebsormidium nitens*; Cr:  
1269 *Chlamydomonas reinhardtii*; Rn: *Rattus norvegicus*; Hs: *Homo sapiens*; Ch: *Chionodraco*  
1270 *hamatus*. (b) Gene structure of *PpAARE1-3* and *AtAARE*. For *PpAARE1* two splice variants exist.  
1271 For *AtAARE* two different 5' UTR definitions are present (upper: Araport11<sup>62</sup>; lower: TAIR10<sup>53</sup>).  
1272 (c) Left: Both splice variants of *PpAARE1* were amplified from complementary DNA (cDNA; +:  
1273 with cDNA template; -: without reverse transcriptase). Expected amplicon size: *PpAARE1\_1*:  
1274 2512 bp; *PpAARE1\_2*: 2596 bp. Primers were designed to be specific for the splice variants  
1275 (Table S1). Right: The longer open reading frame of *AtAARE* was amplified from cDNA. Expected  
1276 amplicon size: 2457 bp (Table S3). (d) Protein structures showing PFAM-domains for *PpAARE1-3*  
1277 and *AtAARE*. All isoforms contain an AARE N-terminal domain (PF19283) and a catalytic  
1278 Peptidase S9 domain (PF00326). *PpAARE1*, *PpAARE2* and *AtAARE* additionally contain a WD40  
1279 domain (PF07676). The long splice variant of *PpAARE1* and the longer open reading frame of  
1280 *AtAARE* encode a predicted N-terminal plastid transit peptide (cTP). AA: amino acid. Cleavable  
1281 N-terminal sequences were predicted by *TargetP2.0*<sup>63</sup>.

1282 **Fig. 2 Confocal microscopy images showing the localization of *PpAARE* isoforms and**  
1283 ***AtAARE* with C-terminal fused eGFP in *Physcomitrella* protoplasts.** Fusion proteins with  
1284 domain structures are depicted. *PpAARE1\_1*, *PpAARE2* and *PpAARE3* localize to the cytoplasm.  
1285 *PpAARE1\_2* localizes to specific foci in plastids (white arrows) and to mitochondria. The N-  
1286 terminal extension of *PpAARE1\_2* encoding a predicted plastid transit peptide (*PpAARE1\_Nt*)  
1287 directs eGFP to plastids and mitochondria. The short variant of *AtAARE* (SV) localizes to the  
1288 cytoplasm. The long variant (LV) localizes to plastids and mitochondria. The N-terminal extension  
1289 of the long variant of *AtAARE* localizes to plastids and mitochondria. Left image: chlorophyll  
1290 autofluorescence (red) and eGFP (green). Middle image: chlorophyll autofluorescence (red) and  
1291 MitoTracker™ (magenta). Right image: chlorophyll autofluorescence (red), eGFP (green),  
1292 Mitotracker™ (magenta) and co-localization of eGFP and MitoTracker™ (white). Bars = 7 μm.

1293 Based on this data, *PpAARE1* is targeted to three organelles: chloroplasts, mitochondria and the  
1294 cytosol. To independently scrutinize these findings, we measured AARE enzyme activity in the

1295 organelles. Using organelle fractionation as previously described<sup>74</sup>, we detected AARE activity in  
1296 chloroplasts, the cytosol, and mitochondria, although to a lesser extent in the latter (Fig. S3).  
1297 Thus, *in vivo* localization of fusion proteins and enzyme measurements after cell fractionation  
1298 independently confirm the predicted triple localization of AARE in *Physcomitrella*.

1299 **Fig. 3 Phenotype analyses, AARE activity and level of oxidized proteins in *Physcomitrella***  
1300 **WT and KO mutants.** (a) Each isoform was knocked out using a different selection marker. The  
1301 selection markers confer resistance against G418 (npt), hygromycin (hpt) and zeocin (zeo),  
1302 respectively. Homologous regions (HR) were chosen in order to remove the full CDS of the  
1303 corresponding gene upon integration of the selection marker. (b) Mean AARE activity on AcAla-  
1304 pNA in *Physcomitrella* protonema with standard deviation (n= three biological replicates).  
1305 Significance levels are based on a one-way Anova and subsequent post-hoc test (\*\*\*: p<0.001)  
1306 and indicate differences compared to WT. (c) Phenotypes of gametophores of WT and the  
1307 different KOs cultivated on KnopME for 4 months. All colonies were grown on the same plate.  
1308 Upper panel: Bar = 0.5 mm; lower panel: Bar = 2mm. (d) Protonema colonies grown on KnopME  
1309 with 0.02% glucose taken from suspension culture. Bar = 1 mm. Images were taken 9 days after  
1310 spotting. (e) Box plot showing the distribution of colony areas (n = 12 colonies per boxplot; colony  
1311 images taken 7 days after spotting). No significant difference of colony areas between WT and  
1312 the KOs was observed (tested via one-way Anova). (f) Box plot showing the number of  
1313 gametophores per colony and day of WT and  $\Delta PpAARE1/2$ . Counting was performed at indicated  
1314 days after spotting protonema suspension culture on solid medium (KnopME with 0.02% glucose).  
1315 Indicated significance levels are based on a two-way Anova with subsequent post-hoc test (\*\*\*:  
1316 p<0.001). The boxplots (e, f) depict the mean (horizontal bold line) of the data, the interquartile  
1317 range (box) and the 1.5x interquartile range (whiskers). (g) Mean AARE exopeptidase activity on  
1318 AcAla-pNA in gametophores. Depicted is the mean of three independent colonies per line with  
1319 standard deviations. All colonies were cultivated on the same plate (Fig. S7a). Significance levels  
1320 are based on one-way Anova and indicate differences compared to WT (\*\*\*: p<0.001). (h) Levels  
1321 of oxidized proteins in gametophores of WT and the different KOs (Coomassie-stained loading  
1322 control is shown in Fig. S7b). The analysis was repeated three times (additional Blots available in  
1323 Fig. S7c, d). Detection of oxidized proteins was performed with the OxyBlot™ *Protein Oxidation*  
1324 *Detection Kit* (Merck).

1325 **Fig. 4 *Physcomitrella* gametophore colonies of varying age.** (a) Colonies of all representative  
1326 knockout mutants after 5 months on solid medium (KnopME). Bar = 5 mm. Gametophores of  
1327  $\Delta PpAARE1/2$  and  $\Delta PpAARE1/3/2$  are only viable at the tip, whereas plant material at the base

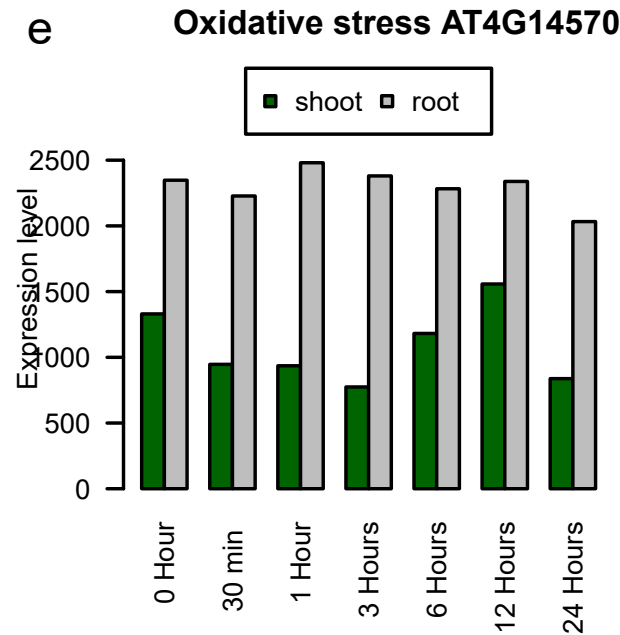
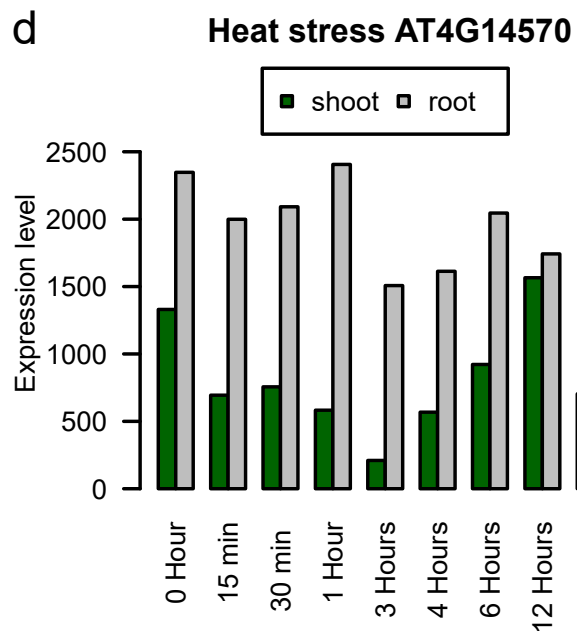
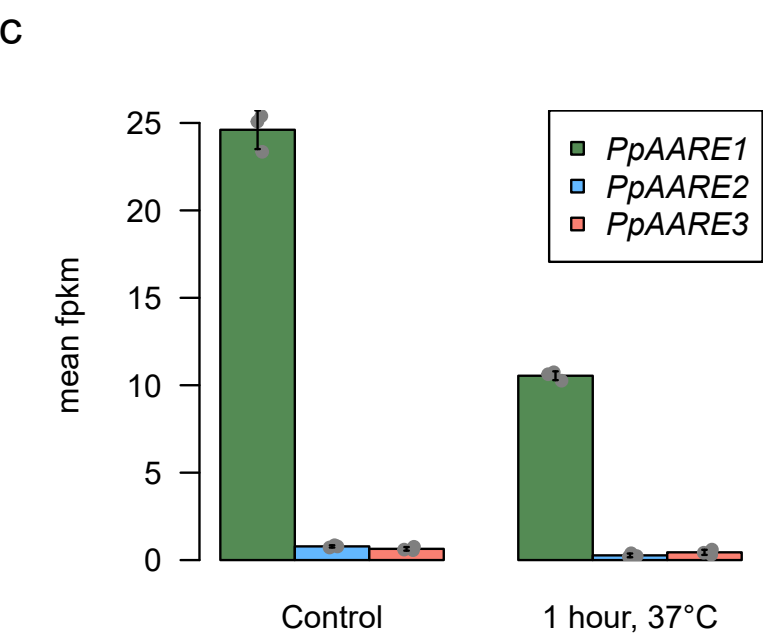
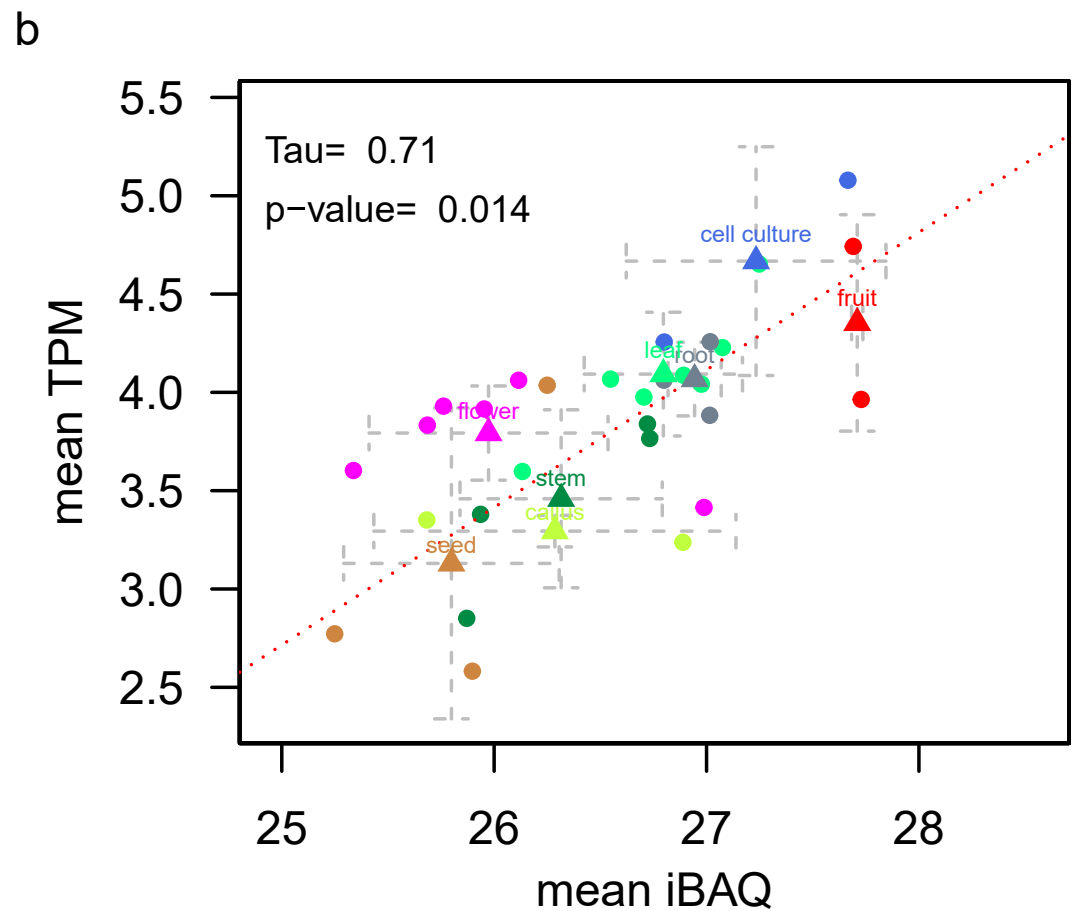
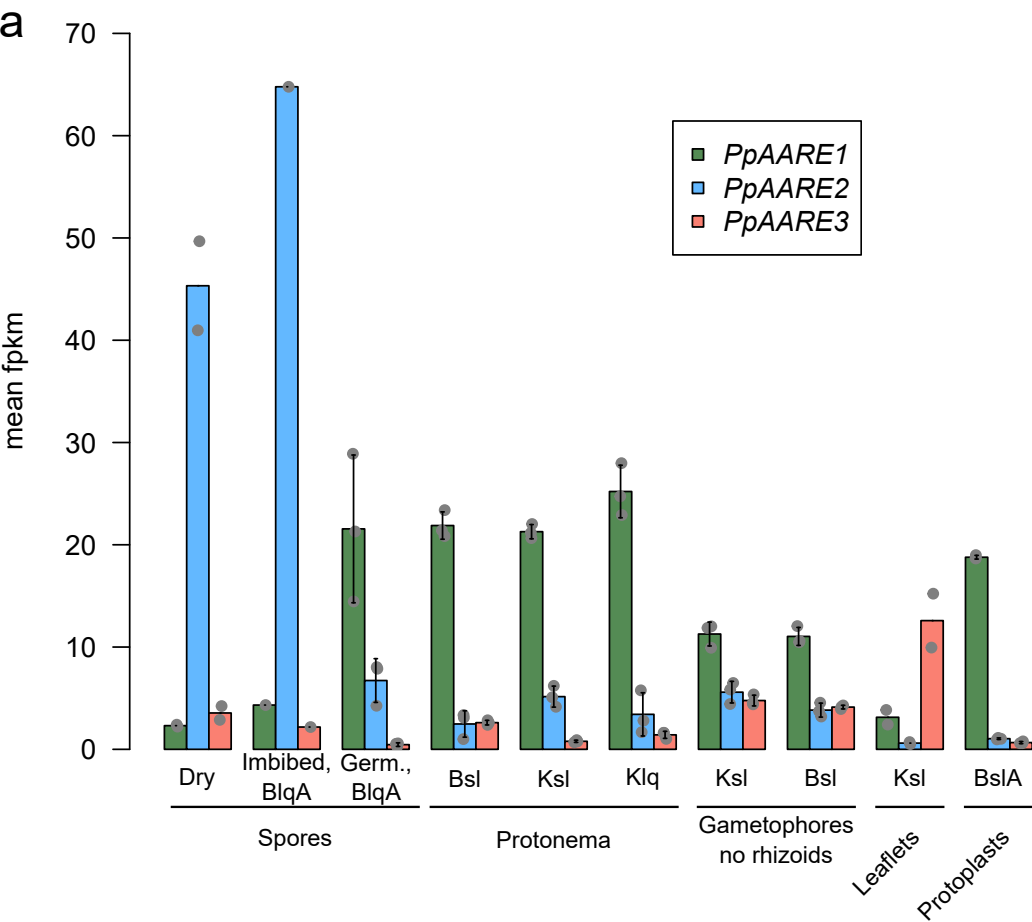
1328 (red arrow) is dead. (b) Colonies after 8 months on solid medium.  $\Delta PpAARE1$  is the parental line  
1329 for  $\Delta PpAARE1/2$ . Gametophores of WT and  $\Delta PpAARE1$  are still viable whereas  $\Delta PpAARE1/2$   
1330 gametophores are mostly dead. Bar = 2 mm. (c) Colonies after 8 months on solid medium.  
1331  $\Delta PpAARE1$  is the parental line for  $\Delta PpAARE1/3$  and  $\Delta PpAARE1/3$  is the parental line for  
1332  $\Delta PpAARE1/3/2$ . Colonies of WT,  $\Delta PpAARE1$  and  $\Delta PpAARE1/3$  still have viable gametophores,  
1333 whereas  $\Delta PpAARE1/3/2$  gametophores are dead. Bar = 2 mm.

1334 **Fig. 5 Reciprocal co-immunoprecipitation (Co-IP) with Citrine-tagged PpAARE isoforms.**  
1335 (a) Tagging of PpAARE isoforms was realized by in-frame fusion with a linker-Citrine CDS at the  
1336 respective native locus *via* homologous recombination. Original stop codons were deleted. (b)  
1337 Volcano plots showing the result of the Co-IPs against each of the PpAARE:Citrine fusion  
1338 proteins. Left panel: Pulldown of PpAARE1:Citrine. Right panel: Pulldown of PpAARE2:Citrine.  
1339 Co-IP was performed with GFP-Trap Magnetic Particles M-270 (Chromotek) and protonema from  
1340 suspension culture. Log<sub>2</sub> ratios of normalized label-free quantitation values (LFQ) are plotted  
1341 against  $-\log_{10}$  of adjusted p-values. Proteins significantly enriched in the Citrine tagged pulldown  
1342 are shown in blue circles ( $p < 0.01$ , FDR = 0.01). Significantly enriched PpAARE isoforms are  
1343 depicted as red crosses.

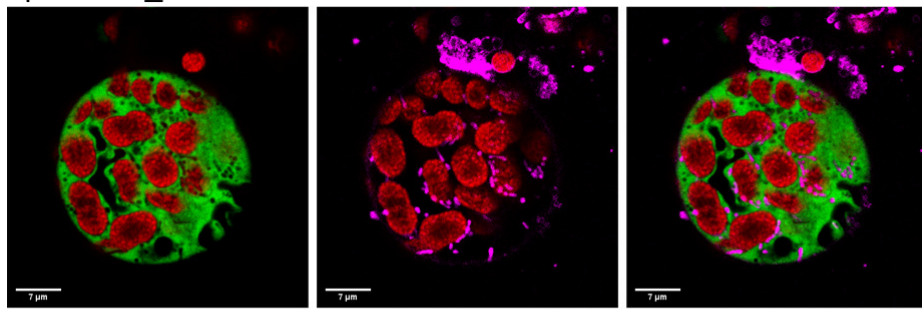
1344 **Fig. 6 Molecular and phenotypical characterization of *A. thaliana* T-DNA mutant lines.** (a)  
1345 Structure of the AtAARE gene and positions of T-DNA insertions (red arrows indicate positions of  
1346 T-DNA insertion, s68 (SALK\_071125) and GK (GK-456A10)) and primers (At1, At2) used for RT-  
1347 PCR (below). Transcription analysis of AtAARE was performed by RT-PCR in WT (Col), s68, and  
1348 GK plants. Negative controls without reverse transcriptase (-), a water control (H<sub>2</sub>O) and genomic  
1349 DNA control (gDNA) are indicated. Expected amplicon sizes: AtAARE: cDNA 739 bp, gDNA: 1204  
1350 bp; PP2AA3 (reference gene): cDNA: 517 bp, gDNA: 911 bp. Primers are listed in Table S3. (b)  
1351 Western blot analysis on extracts of the two T-DNA mutants and WT probed with a polyclonal  
1352 @AARE antibody. In both T-DNA lines AtAARE is not detectable. Full blot images are available  
1353 in Fig. S10. (c) Mean exopeptidase activity in *A. thaliana* extracts on AcAla-pNA and AcLeu-pNA  
1354 with standard deviation (n = 3 biological replicates). Significance levels are based on one-way  
1355 Anova and subsequent post-hoc test (\*\*\*:  $p < 0.001$ ) and indicate differences compared to WT  
1356 (Col). (d) Detection of oxidized proteins in WT (Col) and AtAARE mutant (s68). From three  
1357 independent plants one exterior rosette leaf was taken after cultivation for 8 weeks in short-day  
1358 conditions (8h light/16h dark) Bars correspond to 2 cm. Protein loading control by Coomassie  
1359 staining is depicted below. (e) Boxplot of the bolting analysis of WT (Col, n = 14) and AtAARE  
1360 mutant plants (s68, n=13). The boxplot (e, f) depicts the mean (horizontal bold line) of the data,

1361 the interquartile range (box) and the 1.5x interquartile range (whiskers). Outliers are depicted as  
1362 white dots. Significance level is based on a one-way Anova and subsequent post-hoc test (\*\*\*:  
1363  $p < 0.001$ ). Exemplary plants (45-day-old plants grown in long-day conditions, 16h light/8h dark)  
1364 are depicted below the boxplot. Bars correspond to 1 cm.

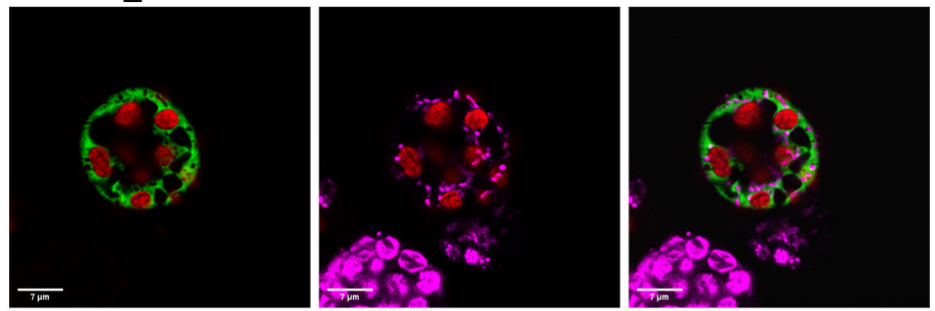
1365



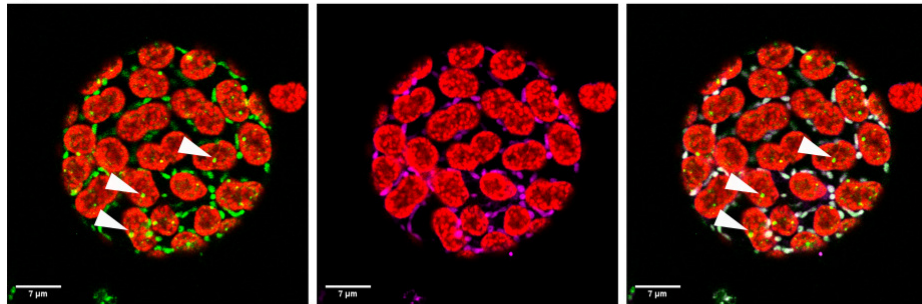
PpAARE1\_1:eGFP



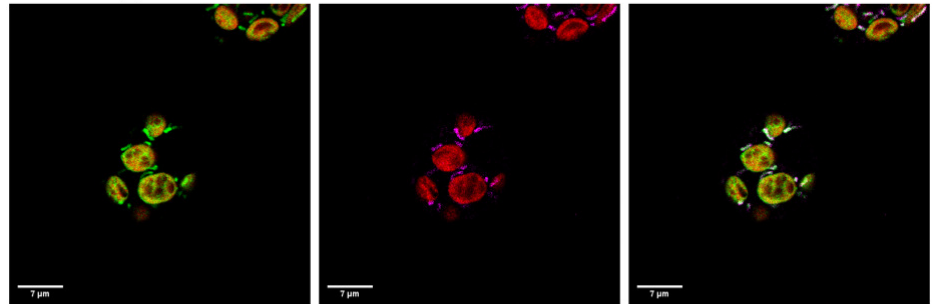
AtAARE\_SV:eGFP



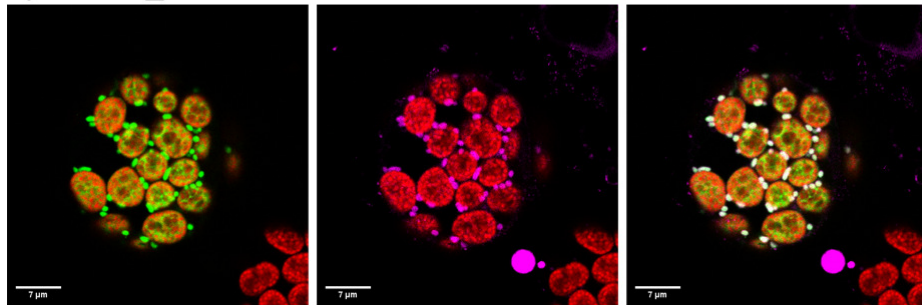
PpAARE1\_2:eGFP



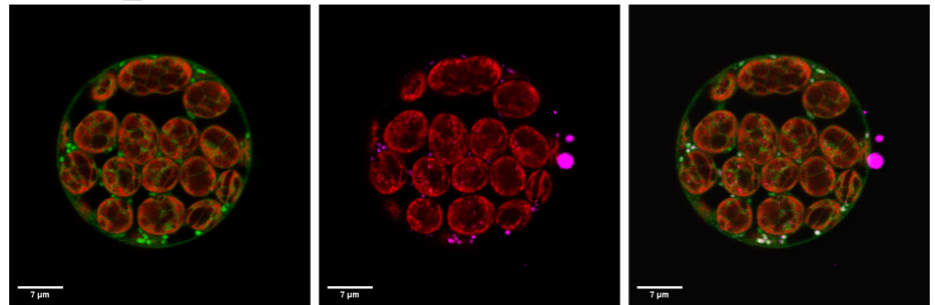
AtAARE\_LV:eGFP



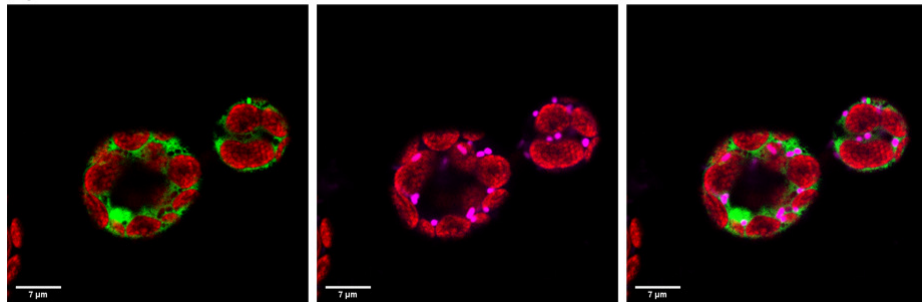
PpAARE1\_Nt:eGFP



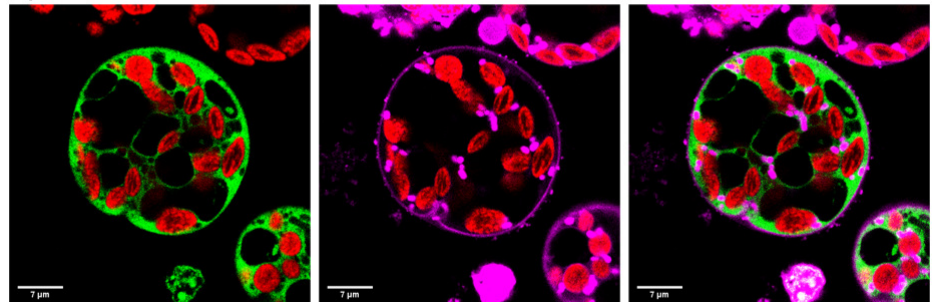
AtAARE\_Nt:eGFP



PpAARE2:eGFP



PpAARE3:eGFP



■ AARE N-terminal domain

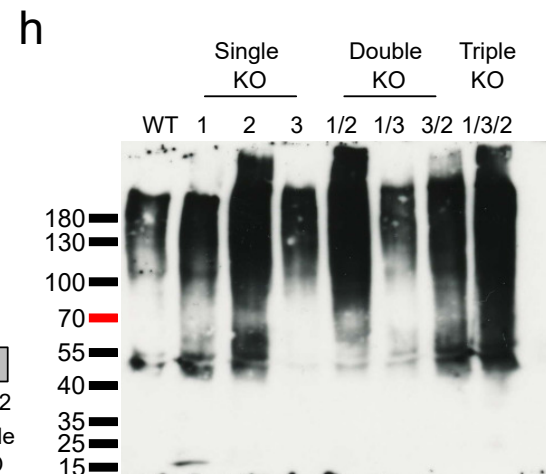
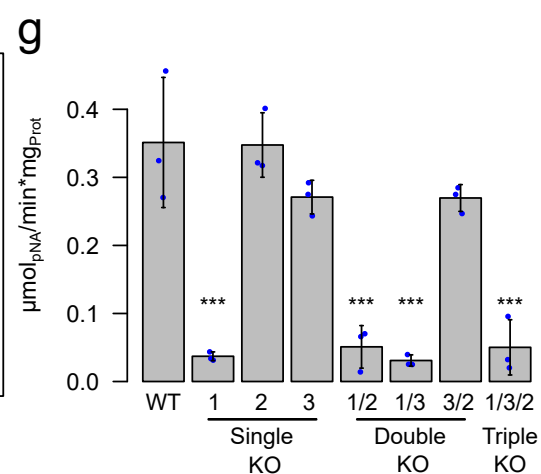
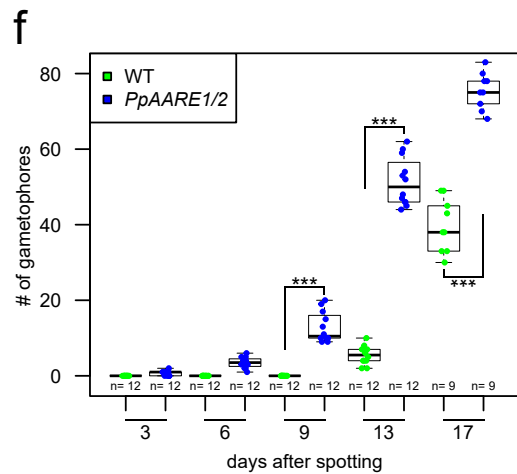
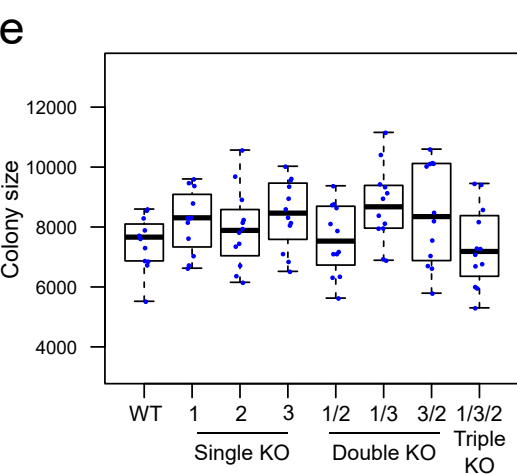
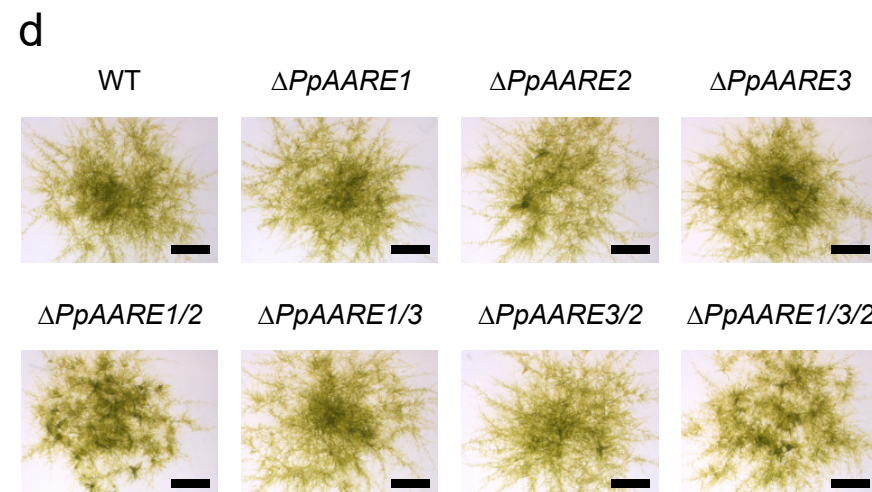
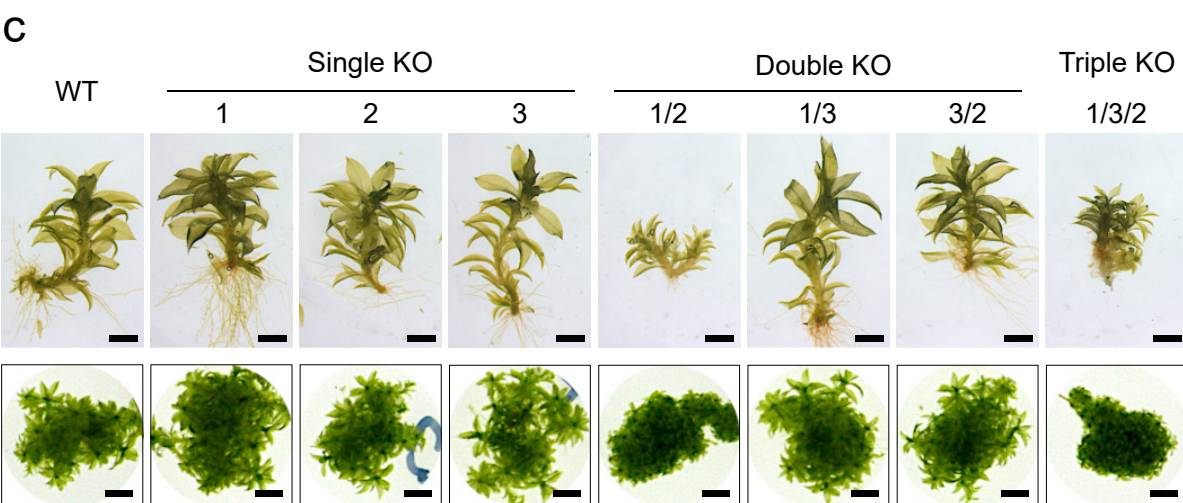
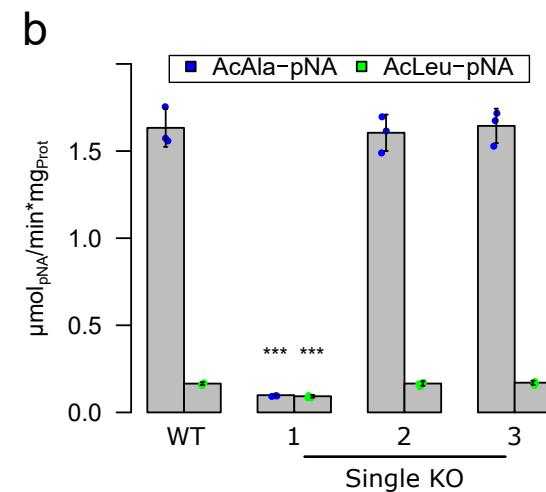
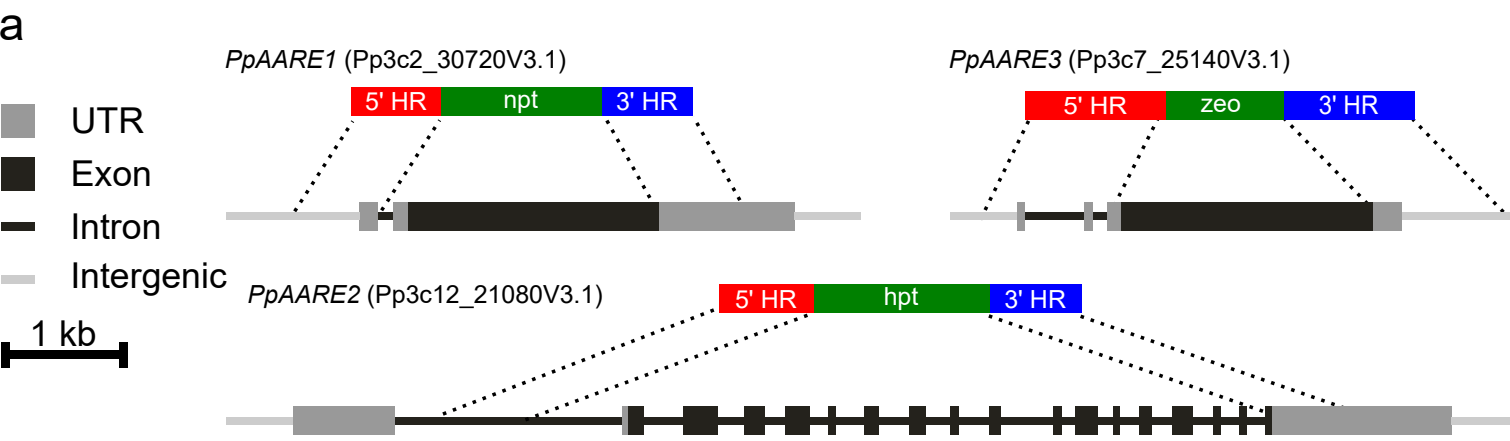
■ WD40 domain

■ S9 Peptidase

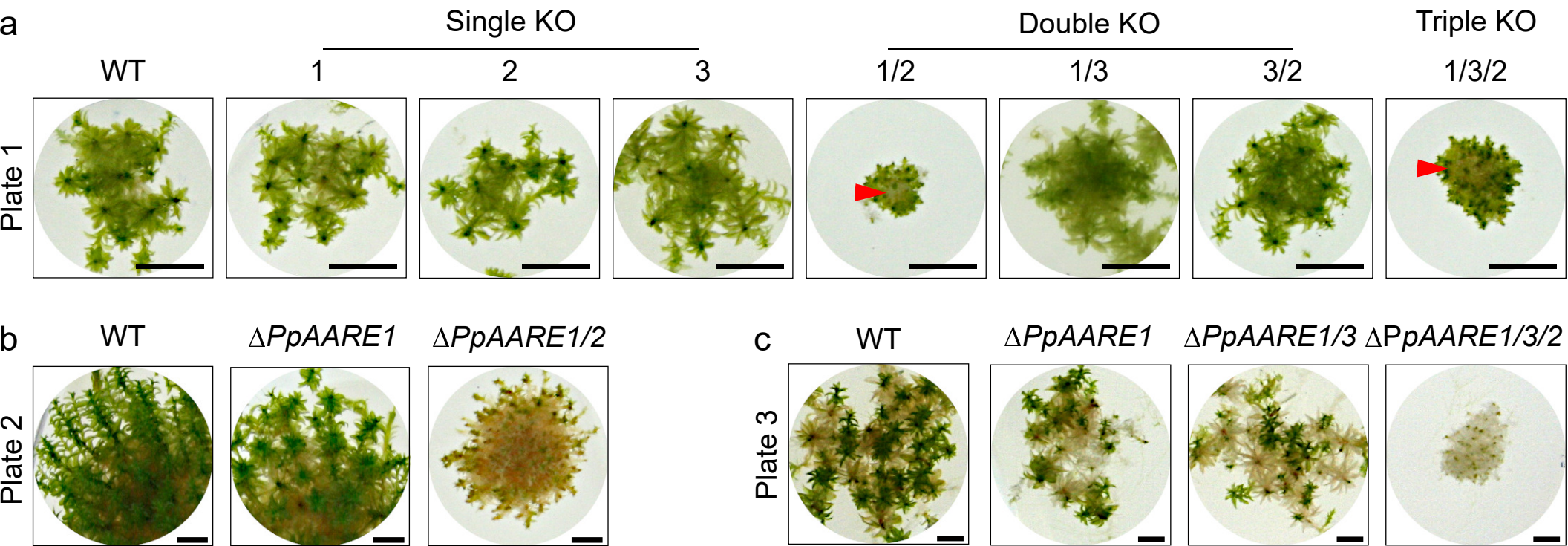
■ Plastid transit peptide

■ GFP

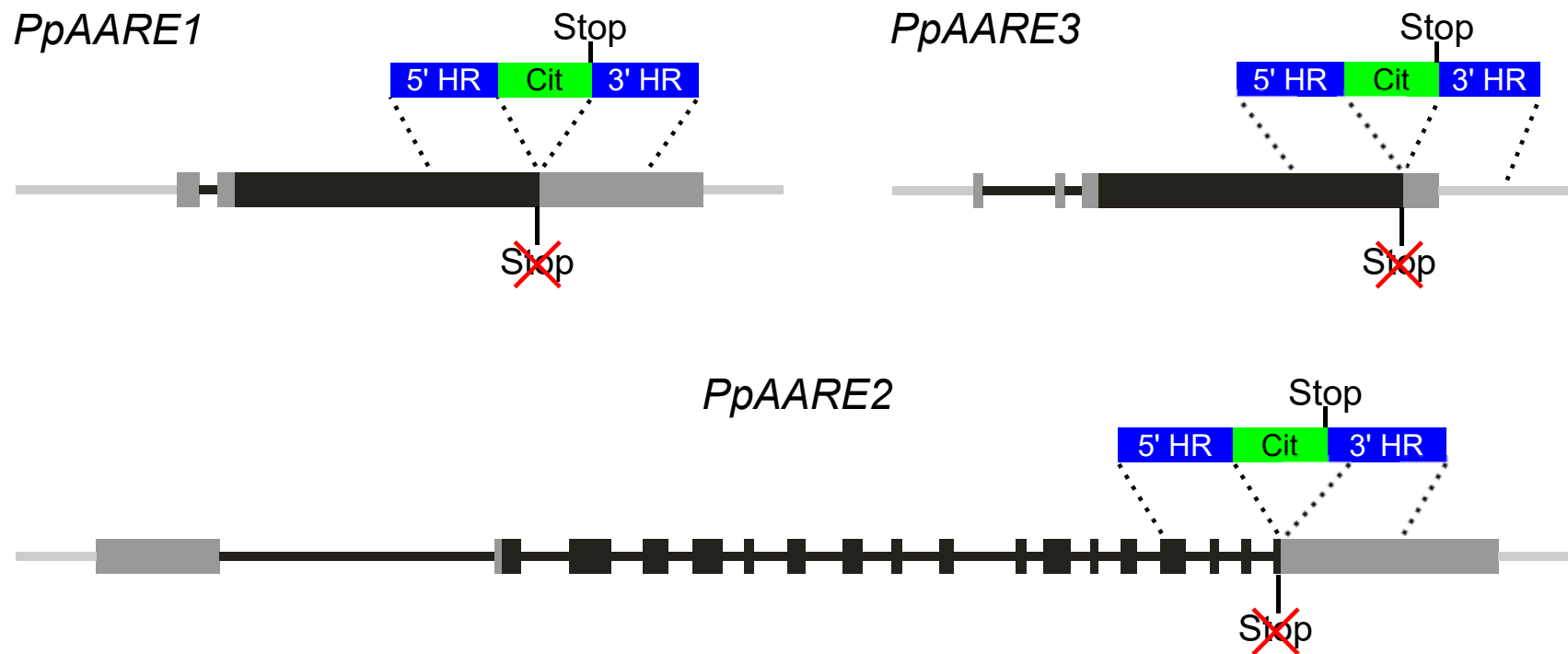
— 50 AA







a UTR Exon Intron Intergenic 1 kb



b

